

Three-Dimensional Battery Architectures

Jeffrey W. Long,^{*,†} Bruce Dunn,^{*,‡} Debra R. Rolison,^{*,†} and Henry S. White^{*,§}

Surface Chemistry Branch, Code 6170, Naval Research Laboratory, Washington, DC 20375, Department of Materials Science and Engineering, UCLA, Los Angeles, California 90095, and Department of Chemistry, University of Utah, Salt Lake City, Utah 84112

Received December 4, 2003

Contents

1. Introduction	4463	5. Structural Characterization of 3-D Electrode Architectures	4478
1.1. Drivers for 3-D Power	4463	5.1. Characterization of the Pore–Solid Architecture	4478
1.2. What Do We Mean by 3-D?	4465	5.1.1. Physisorption	4479
2. Quantitative Advantages of 3-D Cell Architectures	4467	5.1.2. Small-Angle Scattering Techniques	4479
2.1. Overview of Length Scales in 3-D Battery Designs	4467	5.1.3. Electron Microscopy	4479
2.2. Quantifying the Advantages of 3-D Architectures	4467	5.1.4. Scanning Probe Microscopy	4480
2.3. Current Distribution in 3-D Batteries	4469	5.2. Corroboration of Electrochemical Processes with Spectroscopic Techniques	4481
2.3.1. Interdigitated Electrode Arrays	4469	6. Fabrication En Route to 3-D Integration of Architectural Components	4483
2.3.2. Plate, Tubule, and Aperiodic 3-D Architectures	4470	6.1. Micromachining	4483
2.4. Overall Design Issues	4470	6.1.1. Carbon MEMS (C-MEMS)	4483
2.5. Cathodes and Anodes Separated by Nanometer-Wide Electrolytes	4470	6.1.2. Micromachining of Silicon Molds	4484
3. Prior Examples of Small Power	4471	6.2. 3-D Fabrication Based on 2-D Structures: Origami	4485
3.1. Scope of Small Power	4471	7. Advances toward Integration of Active Components into a 3-D Battery	4486
3.2. Miniaturizing Microreactors and Fuel Cells	4471	7.1. Present Status	4486
3.2.1. Compact Mixed Reactors	4471	7.2. Electrodeposition of Dielectrics—Separators and Cation-Conductive Electrolytes	4486
3.2.2. Microfabrication Approaches for Small Power	4472	7.3. Hybrid Polymer–Aerogel Nanoarchitectures as Electrochemical Capacitors	4487
3.2.3. Membraneless Opportunities with Laminar Flow in Microfluidic Reactors	4472	7.4. Solid-State Electrical Characterization of Conformal, Ultrathin Polymer Dielectrics	4487
3.2.4. Power in Vivo and Biologically Derived	4472	7.5. Ultrathin Polymer Electrolyte—Leakage Currents	4488
3.3. Thin-Film Batteries	4473	7.6. Last Step: Add an Interpenetrating Anode	4488
3.4. Generating Power from Ambient Sources	4474	7.7. Packaging of 3-D Batteries	4489
3.5. Hybrid Micropower	4474	8. Conclusions	4489
4. Component Design for 3-D Battery Structures	4474	9. Acknowledgments	4489
4.1. Thinking Like Architects	4474	10. References	4489
4.2. Porous Membranes as Structure-Directing Templates	4475		
4.3. Template Synthesis of Ordered Macroporous Solids with Colloidal Crystals	4476		
4.4. Template Synthesis of Mesoporous Solids with Supramolecular Assemblies	4476		
4.5. Hierarchical Designs Based on Templating Strategies	4477		
4.6. Aerogels and Related Nanostructures—Aperiodic Pore–Solid Architectures	4478		

1. Introduction

1.1. Drivers for 3-D Power

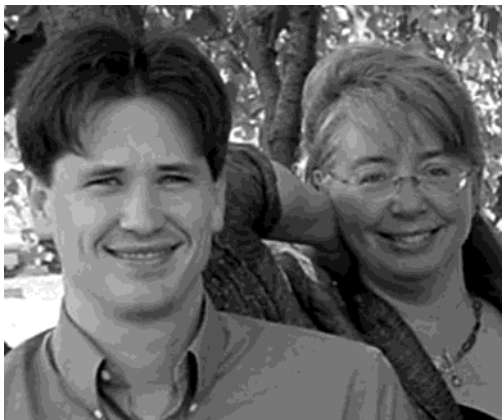
The worldwide thirst for portable consumer electronics in the 1990s had an enormous impact on portable power. Lithium ion batteries, in which lithium ions shuttle between an insertion cathode (e.g., LiCoO_2) and an insertion anode (e.g., carbon), emerged as the power source of choice for the high-performance rechargeable-battery market. The performance advantages were so significant that lithium ion batteries not only replaced Ni–Cd batteries but left the purported successor technology, nickel–metal hydride, in its wake.¹ The thick metal plates of

* To whom correspondence should be addressed. J.W.L.: e-mail, jwlong@ccs.nrl.navy.mil; telephone, (+1)202-404-8697. B.D.: e-mail, bdunn@ucla.edu; telephone, (+1)310-825-1519. D.R.R.: e-mail, rolison@nrl.navy.mil; telephone, (+1)202-767-3617. H.S.W.: e-mail, white@chem.utah.edu; telephone, (+1)810-585-6256.

† Naval Research Laboratory.

‡ UCLA.

§ University of Utah.



Jeffrey Long (left) was born in Great Falls, Montana in 1970, but he spent most of his early years in Winston-Salem, NC. He received a B.S. in Chemistry with Honors from Wake Forest University in 1992. Working with Prof. Royce Murray, he earned a Ph.D. in Chemistry from the University of North Carolina at Chapel Hill in 1997. His research focuses on nanostructured materials, particularly hybrid nanoarchitectures for applications in sensing, separations, and electrochemical energy storage and conversion.

Debra Rolison (right) was born in Sioux City, Iowa in 1954. She received a B.S. in Chemistry from Florida Atlantic University in 1975 and a Ph.D. in Chemistry from the University of North Carolina at Chapel Hill in 1980 under the direction of Prof. Royce W. Murray. She joined the Naval Research Laboratory as a research chemist in 1980 and currently heads the Advanced Electrochemical Materials section. She is also an Adjunct Professor of Chemistry at the University of Utah. Her research at the NRL focuses on multifunctional nanoarchitectures, with special emphasis on new nanostructured materials for catalytic chemistries, energy storage and conversion, biomolecular composites, porous magnets, and sensors.

traditional batteries gave way to lithium ion cells in which the anode, separator/electrolyte, and cathode were stacked, spiral wound, or folded.² Although the materials in today's batteries differ from those of the displaced technologies and the energy density of the electrochemical cell is decidedly larger, the basic two-dimensional (2-D) character and layer-by-layer construction of the cell remains intact. The next generation of lithium ion-polymer electrolyte batteries will offer improvements in gravimetric and volumetric energy densities (Wh g^{-1} and Wh L^{-1} , respectively), but the same configurations will prevail.³

Another massive market force is expected to develop over the next decade in the area generally known as microelectromechanical systems or MEMS.⁴ This field grew out of the integrated-circuits (IC) industry, and in less than a decade, MEMS devices successfully established high-volume commercial markets for accelerometers and pressure sensors in the automotive industry, ink-jet print heads, and digital micromirrors for image projection. By 2001, the global market for MEMS was nearly \$14 billion.⁵ Developments in the MEMS field seem to be continual, and MEMS devices are beginning to make significant contributions in new arenas, including fluidics, wireless communications, sensors, and optics.⁶⁻⁹ The rapid expansion of MEMS into new areas is due to the development of surface micromachining techniques, which involve photolithographic patterning, deposition, and selective etching of multilayered films to form device structures.¹⁰

There is tacit recognition that power is a vital issue for the continued development of the MEMS device



Bruce Dunn holds the Nippon Sheet Glass Chair in Materials Science & Engineering at UCLA. He received his B.S. at Rutgers University and his M.S. and Ph.D. degrees at UCLA. He was a staff scientist at the General Electric Corporate Research and Development Center before joining the UCLA faculty in 1980. His research interests concern the synthesis of ceramics and inorganic materials and characterization of their electrical, electrochemical, and optical properties. A continuing theme in his research is the use of sol-gel methods to synthesize materials that incorporate specific dopants and are capable of developing unique microstructures and properties. The areas presently being studied in his group include biosensors, intercalation compounds, aerogels, and organic/inorganic hybrid materials.



Henry White was born in Chapel Hill, North Carolina in 1956. He received a B.S. in Chemistry from the University of North Carolina in 1978 and a Ph.D. in Chemistry from the University of Texas at Austin in 1982. He held a postdoctoral appointment at the Massachusetts Institute of Technology from 1983 to 1984 and was on the faculty of the Department of Chemical Engineering and Materials Science at the University of Minnesota from 1984 to 1993. He is currently a Professor of Chemistry at the University of Utah. His research interests include magnetic-field-induced transport, oxide films and corrosion, iontophoretic transdermal drug delivery, and electrochemical phenomena at electrodes of nanometer dimensions.

field. In particular, the issue of how to power MEMS-based sensors and actuators has been largely neglected.¹¹ While a conventional macroscopic power supply could be employed for these devices, the prospect of powering arrays of micromachined sensors and actuators is likely to lead to interconnection problems, cross-talk, noise, and difficulty in controlling the power delivered. In contrast, the complexity of power delivery is reduced if one were to design the power supply to be of the same dimensional scale as the sensors and actuators. Specifically, site-specific power can be realized, and improvements in noise and power efficiency may be achieved.

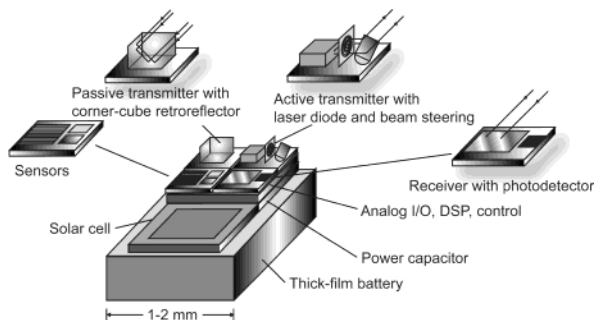


Figure 1. Smart dust mote and its components: Micro-fabricated sensors, optical receiver, signal-processing and control circuitry; the power source consists of a solar cell and a thick-film battery. (Derived with permission from ref 16. Copyright 2001 IEEE)

The power needs for MEMS devices are diverse—and batteries may not be the best choice to provide power to systems based on various types of MEMS drives. For example, magnetic drives operate at less than 1 V, but they require generating hundreds of milliamperes, which becomes a difficult challenge for batteries sized on the subcentimeter scale. The required micro- to nanoampere current levels for electrostatic and piezoelectric MEMS are feasible for batteries, but the tens to hundreds of volts that are needed will present difficulties for batteries with nominal voltages of 3 V. However, there may be a niche for batteries that would be used to power 10–15 V drives.

A more reasonable application for batteries is in the area of MEMS-based sensing. In one particularly exciting direction, batteries supply power to autonomous nodes, with each node containing one or more sensors, along with powering the computation and communication capabilities necessary to relay the findings of each node.¹² One approach, “smart dust”, represents an excellent example where integrated batteries may contribute; the basic device is shown in Figure 1. The device integrates into a single package, MEMS components (sensors, beam steering), optical communication components (optical receiver, semiconductor laser diode), signal-processing and control circuitry, and a power source based on batteries and solar cells, in a volume on the order of a cubic millimeter.

A calculation of the power requirements of the smart dust mote underscores our point that the present generation of batteries cannot effectively power this device. Thin-film batteries are among the most advanced of the lithium battery systems, with a capability to scale down to dimensions on the same order of magnitude as the cubic millimeter of the dust mote.¹³ The energy density for the thin-film system is $\sim 2 \text{ J mm}^{-3}$,¹⁴ which matches or exceeds standard lithium ion systems, such as those that power laptop computers. A key design requirement for the smart dust mote is that the power consumption cannot exceed $10 \mu\text{W}$. If the dust mote uses this power continuously over a day, it will consume $\sim 1 \text{ J}$.

Can a thin-film battery supply the 1 J per day of energy necessary to power a smart dust mote? At first glance, it would appear that there should be no problem; the device consumes 1 J mm^{-3} and the

battery is able to supply 2 J mm^{-3} . The reality, however, is that thin-film batteries are 2-D devices. Such batteries are necessarily thin in order to prevent power losses typically associated with the slow transport of ions, but a practical limitation arises from the fracture of cathode films that get too thick ($> 2 \mu\text{m}$), which leads to low capacity per square millimeter. With a typical device thickness on the order of $15 \mu\text{m}$, a thin-film battery requires a significant amount of area in order to supply 2 J mm^{-3} .

The real question becomes whether a thin-film battery can supply what the smart dust mote requires within the constraints of the areal “footprint” available for the battery on the smart dust mote—1 J of energy over 1 mm^2 of “real estate.” The traditional yardsticks by which battery energy and power are normalized are weight and volume [i.e., gravimetric and volumetric energy (and power) densities]. These metrics are no longer sufficient when one considers portable power for small devices: such devices have limited area available to integrate components into a system. For this reason it is important to establish the effective area of the power source, its footprint, and to normalize the available energy (and/or power) to this area.

The energy per unit area as reported for several lithium thin-film batteries ranges from 0.25 to $\sim 2 \times 10^{-2} \text{ J mm}^{-2}$.¹⁵ Thus, thin-film batteries, despite their excellent energy per unit volume, fall far short of being able to power a smart dust mote for 1 day. If the areal footprint were made 100 times larger (at 1 cm^2), the thin-film approach would be acceptable. The consequences of the 2-D nature of thin-film batteries are easily overlooked. The calculation by Koeneman et al. ignored the 2-D character of thin-film batteries when they concluded that these batteries could carry out some 60 000 actuations of a “smart bearing”.¹¹ When one considers the actual area available for the power source on the device, only about 1200 actuations are possible.

Smart dust motes are not just intriguing lab toys but successfully demonstrated devices.¹⁶ However, because of the inability to obtain scale-appropriate lithium ion batteries, the first devices tested were powered with hearing-aid batteries. The example of the smart dust mote illustrates a critical issue concerning all small power designs and their effective integration on-board the device. To power devices with limited real estate and maintain a small areal footprint, batteries must somehow make good use of thickness. Three-dimensional configurations offer a means to keep transport distances short and yet provide enough material such that the batteries can power MEMS devices for extended periods of time. The detailed calculations discussed in section 2 show that batteries configured as 3-D structures can readily achieve the 1 J mm^{-2} areal footprint required to power the smart dust mote.

1.2. What Do We Mean by 3-D?

Lithium ion batteries use insertion processes for both the positive and negative electrodes, leading to the term “rocking chair” battery.¹ The resulting transport of Li ions between the electrodes, usually

arranged in a parallel-plate configuration, is 1-D in nature. To minimize power losses resulting from slow transport of ions, the thickness of the insertion electrodes, as well as the separation distance between them, is kept as small as possible. This approach may appear counterintuitive in the effort to produce a useful battery, because reducing the thickness of the electrode results in lower energy capacity and shorter operating time. Thus, battery design always trades off between available energy and the ability to release this energy without internal power losses.

In recent years there has been the realization that improved battery performance can be achieved by reconfiguring the electrode materials currently employed in 2-D batteries into 3-D architectures. Some of the envisioned approaches are reviewed in more detail in section 2. The general strategy of this approach is to design cell structures that maximize power and energy density yet maintain short ion transport distances. While many possible architectures can achieve this goal, a defining characteristic of 3-D batteries is that transport between electrodes remains one-dimensional (or nearly so) at the microscopic level, while the electrodes are configured in complex geometries (i.e., nonplanar) in order to increase the energy density of the cell within the footprint area. A 3-D matrix of electrodes (in a periodic array or an aperiodic ensemble) is necessary to meet both the requirements of short transport lengths and large energy capacity. Improvements in energy per unit area and high-rate discharge capabilities are two of the benefits that may be realized for these 3-D cells.

Perhaps the most obvious 3-D design is that consisting of interdigitated electrodes shown in Figure 2a. This prototype configuration is used in modeling studies, the results of which are reviewed in section 2. The anode and cathode consist of arrays of rods separated by a continuous electrolyte phase. The spatial arrangement of the anode and cathode arrays determines the current–potential distribution. Clearly, the short transport distances lead to a much lower interelectrode ohmic resistance as compared to traditional planar battery configurations.

A central feature for the interdigitated configuration is that the arrays need to be periodic. A variation on this approach is to use interdigitated plates rather than rods (Figure 2b), which is analogous to stacking 2-D batteries with parallel connection.

There is no particular reason that the electrolyte must serve as the continuous phase in 3-D battery architectures. Another 3-D design utilizes a concentric arrangement where the rod array is composed of one of the active electrode materials and is then coated by an electrolyte layer. The other electrode material then fills the remaining free volume and serves as the continuous phase, as shown in Figure 2c. As was discussed for the above battery configurations, short transport distances between the insertion electrodes lead to low ohmic resistance. Although a periodic arrangement is shown in Figure 2c, it is not clear at the present time whether this is beneficial or not with respect to the current–potential distribution. Relaxing the periodicity condition may be an

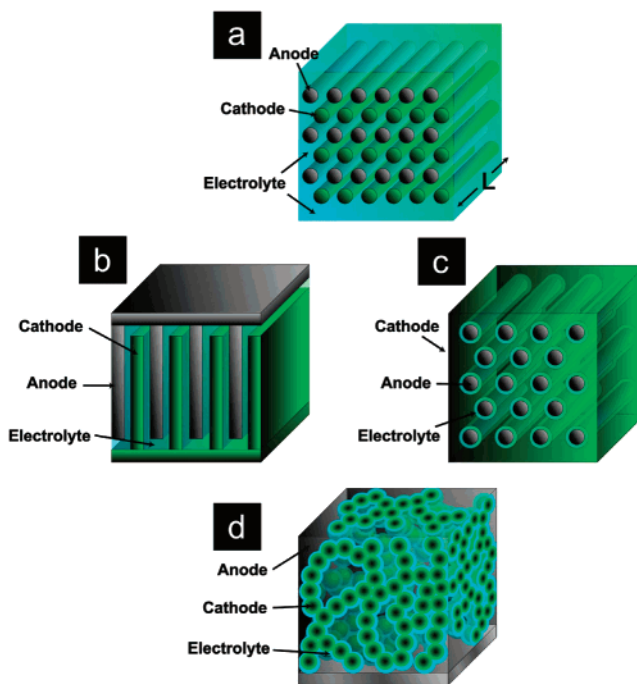


Figure 2. Examples of prospective 3-D architectures for charge-insertion batteries: (a) array of interdigitated cylindrical cathodes and anodes; (b) interdigitated plate array of cathodes and anodes; (c) rod array of cylindrical anodes coated with a thin layer of ion-conducting dielectric (electrolyte) with the remaining free volume filled with the cathode material; (d) aperiodic “sponge” architectures in which the solid network of the sponge serves as the charge-insertion cathode, which is coated with an ultrathin layer of ion-conducting dielectric (electrolyte), and the remaining free volume is filled with an interpenetrating, continuous anode.

important consideration, because prospective synthetic techniques, such as templating through mesoporous membranes, do not necessarily produce periodic arrays.

A completely aperiodic 3-D battery configuration is the “sponge” approach, where the electrolyte layer is formed around a random 3-D network of electrode material (Figure 2d). This design strategy also represents a concentric configuration in that the electrolyte envelops the electrode material while the other electrode material fills the mesoporous and macroporous spaces and surrounds the electrolyte. Short transport-path characteristics between the insertion electrodes are preserved with this arrangement. In contrast to the other 3-D designs, all battery components— anode, cathode, and electrolyte—are continuous throughout the sponge structure.

The above discussion provides the context for 3-D batteries. That is, there are a variety of small power applications, typified by MEMS devices, which the most advanced, 2-D lithium battery systems are unable to satisfy. The inability to provide sufficient power is because of configuration and not because of intrinsic energy density. Three-dimensional designs offer the opportunity to achieve milliwatt-hour energies in cubic millimeter packages and, more importantly, with square millimeter footprints. While such power sources may not influence the enormous commercial markets in cell phones and laptop computers, they are certain to impact emerging markets where

integrated power is required for communication, sensing, and networking.

This paper discusses the prospects for creating 3-D architectures for batteries. We next introduce calculations for the 3-D interdigitated array battery (Figure 2a), which will illustrate the design considerations under which the 3-D configuration leads to better performance than the conventional 2-D one. Other sections then discuss the prior art in small power, followed by the materials, synthetic, and fabrication approaches required to achieve 3-D designs. Finally, we review the present status of the systems most likely to demonstrate true 3-D battery operation.

2. Quantitative Advantages of 3-D Cell Architectures

2.1. Overview of Length Scales in 3-D Battery Designs

The four architectures introduced in Figure 2 have wide-ranging length scales and geometries that are largely dictated by their respective methods of fabrication. These length scales and geometries will determine the performance characteristics of 3-D batteries based on these architectures. Thus, before attempting to quantify some of the advantages (as well as the disadvantages) of 3-D cells, a brief overview is presented of the methods of fabrication currently employed, with emphasis on the resulting geometrical and scale differences. Detailed descriptions of the fabrication procedures are presented in section 4.

At present, only the individual component arrays (i.e., individual cathode or anode arrays) of the periodic interdigitated electrode cell (Figure 2a) have been fabricated using lithographic methods. The results of these limited efforts, however, provide a rough guide to what is possible in battery design within the microlithographic laboratory. Typically, the electrodes are cylindrical rods with diameters ranging from 5 to 100 μm and lengths from 10 to 200 μm . For instance, Madou and co-workers have fabricated an array of cylindrical carbon electrodes with $\sim 10\text{-}\mu\text{m}$ diameter and $\sim 200\text{-}\mu\text{m}$ length.¹⁷ Lithographic fabrication methods also allow other geometries beyond cylinders to be considered (e.g., triangular rods). It is most probable that the use of current lithographic methods will continue to yield structures with lateral dimensions (i.e., electrode diameter and electrode-to-electrode spacing) on the micrometer length scales, with more emphasis placed on increasing the length of the electrode, L , to achieve high aspect ratios. This strategy yields the high areal energy capacity that drives the interest in 3-D designs (vide infra). Other periodic arrays, such as those based on the use of origami to “unfold” an array of lithographically designed cathodes and anodes on a base support¹⁸ and of arrays of plates (Figure 2b), are also envisioned at the micrometer length scale. Smaller lateral dimensions will likely be obtained in the future with advances in lithographic methods.

One disadvantage of all periodic interdigitated electrode cells is that the primary current distribu-

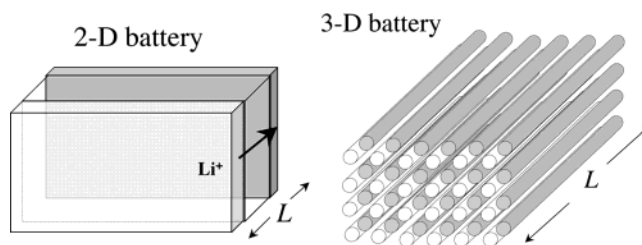


Figure 3. 2-D parallel-plate and 3-D interdigitated-array batteries.

tion is nonuniform.¹⁹ This nonuniformity can be readily recognized by inspection of Figure 2a and realizing that the distance between the anodes and cathodes is variable along the circumference on any individual electrode. A quantitative description of this issue is discussed below.

The concentric tubule arrays and aperiodic continuous sponge architectures are based on *conformal deposition methods*, in which layers of electrolyte and/or electrode materials are sequentially^{20–23} or simultaneously assembled within an array of pores in a membrane (Figure 2c) or in an aperiodic array (Figure 2d). Film deposition methods (see section 7) can yield electrode and electrolyte films of nanometer thicknesses, and in fact, a prototype of the aperiodic architecture has been recently reported.^{20–23} Thus it is possible to envision batteries soon in which the cathode and anode are separated by 10 nm. However, at these distances, the physical structure of the interface must be exceedingly stable to prevent shorting of the electrodes. In addition, electrostatic interactions between the cathode and anode (i.e., “overlapping” double layers) and exceedingly fast transport rates within the separator will undoubtedly influence the current–voltage curves in complex ways that are just now being investigated.²⁴ One key advantage of these 3-D architectures (and unlike the periodic interdigitated array) is that the current density across the electrode surfaces is uniform.

2.2. Quantifying the Advantages of 3-D Architectures

As discussed in section 1, the key advantage associated with the proposed 3-D battery structures is the ability to achieve large areal energy capacities without making sacrifices in power density that may result from slow interfacial kinetics (associated with a small electrode area-to-volume ratio) and/or ohmic potential losses (associated with long transport distances). This argument is now quantitatively demonstrated in the following paragraphs for the 3-D interdigitated electrode array shown in Figure 2a.

To facilitate a demonstration of the advantages of the 3-D architecture, we quantitatively compare metrics related to performance (e.g., areal energy capacity, active surface area) of a conventional 2-D parallel-plate design with the 3-D interdigitated array cell (Figure 3). We assume a thin-film 2-D battery that comprises a 1-cm²-area anode and cathode, each 22.5- μm -thick and separated by a 5- μm -thick electrolyte. The total volume of electrodes and separator is 5×10^{-3} cm³ (the cell housing is ignored for simplicity, but is expected to be a comparable

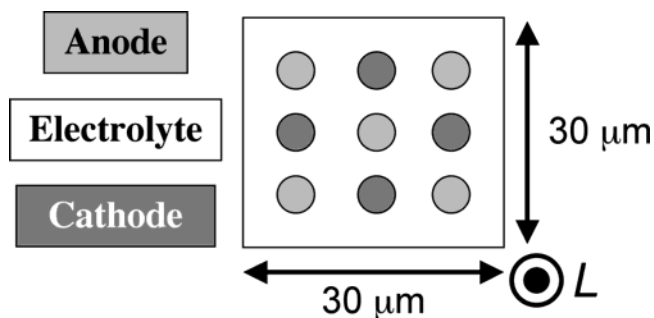


Figure 4. Square array of interdigitated anodes and cathodes.

percentage of the total volume in both 2-D and 3-D designs).

It is relatively straightforward to show that a corresponding 3-D square-array battery (Figure 4) with the same total volume (i.e., $5 \times 10^{-3} \text{ cm}^3$), constructed from $5\text{-}\mu\text{m}$ -radius cathode and anodes that are separated (center to center) by $10 \mu\text{m}$, contains $\sim 39\%$ of the energy capacity of the thin-film design. Clearly, the lower energy capacity is due to a higher percentage of the total volume being occupied by the electrolyte. While the energy capacity of the 3-D design varies with the shape and arrangement of the electrodes, it will always be lower than that of the 2-D design for equal total volumes.

There are several intriguing advantages of the 3-D design that are not reflected in the above numbers. For instance, the active cathode and anode surface areas in the 3-D design are 3.5 cm^2 each, significantly larger than the 2-D design (1 cm^2). This difference favors the 3-D design through a reduction in interfacial kinetic overpotential, which is inversely proportional to the electrode area. In addition, the distance that ions must be transported in discharging the 2-D battery is 350% larger than in the 3-D design. Thus, in principle, the 3-D design is significantly less susceptible to ohmic losses and other transport limitations. To achieve equal transport length scales in the 2-D design (i.e., by decreasing the electrode thickness to $5 \mu\text{m}$) would require a 330% increase in the areal footprint in order to maintain equal cell volume, a significant disadvantage in employing these devices in MEMS and microelectronic applications.

While the above comparison of 2-D and 3-D designs indicates that the 3-D battery has inherently lower energy capacity per total cell volume, in fact, the capacity of the 3-D design can be increased without limit by increasing L , without sacrificing the small areal footprint or high power density. As shown in Figure 5, for the same areal footprint, i.e., 1 cm^2 , the above square array 3-D design with $L = 500 \mu\text{m}$ has a capacity that is 350% larger than the 2-D design. Such a microbattery would contain 222 222 cathodes and 222 222 anodes, with $\sim 35 \text{ cm}^2$ each of active cathode and anode area!

Clearly L cannot be increased without limit, as the ohmic resistance of the electrodes will become sufficiently large to offset the advantages of increased areal capacity. While this problem has not been treated systematically, it is clear that the optimized value of L will be determined by the electronic

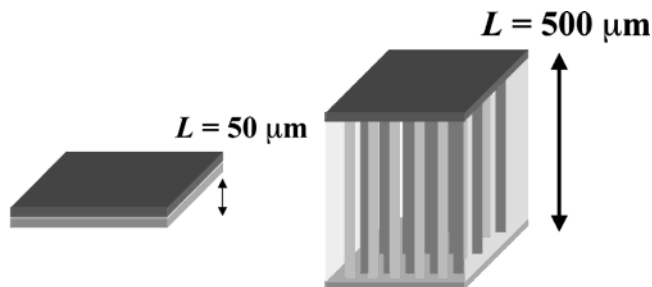


Figure 5. An increase in the height of the interdigitated 3-D battery, L , results in increased areal energy capacity and electrode area, without an increase in transport distances.

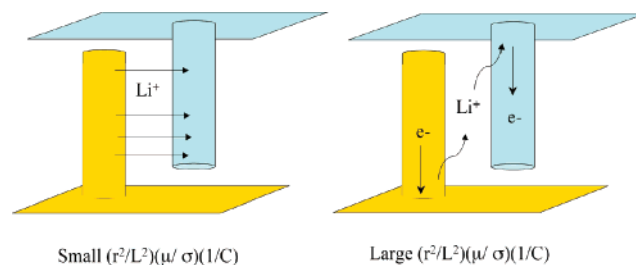


Figure 6. Dependence of electrode utilization on electrode conductivity (σ) and ion diffusivity (D). L and r are the length and radius of the electrodes, respectively.

conductivity of the electrode materials (σ) and the ionic conductivity of the electrodes and electrolyte, in addition to the electrode geometry, as indicated in Figure 6.

The dimensionless number $U = (r^2/L^2)(\mu/\sigma)(1/C)$, where r is the radius of the electrode, μ is ionic mobility of cations (Li^+), and C is the volumetric energy capacity (C/cm^3), is a quantitative measure of uniformity of current across the 3-D electrode surfaces and, thus, whether the electrode material is uniformly utilized during cell charging and discharging. Decreasing U corresponds to a more uniform current distribution along the length of the electrode. This scenario is a desired one, as long as the decrease in U results from high electronic conductivity in the electrodes (i.e., large σ), rather than low ionic conductivity in the electrolyte (i.e., small μ). Increasing U corresponds to a more nonuniform discharge of the electrodes, which may result in underutilization of the electrode materials during rapid discharge, as well as increasing stress along the length of the electrodes. Similarly, $U = (w^2/h^2)(\mu/\sigma)(1/C)$ for a rectangular electrode in the interdigitated plate design (Figure 2b), where w is the electrode thickness and h is the electrode height measured from the base. Clearly, numerical values of U will depend on electrode geometry and materials.

The arguments developed in this section apply to all of the potential 3-D designs shown in Figure 2. In each design, an increase in areal energy capacity can be obtained by simply increasing L , without any loss of power density due to interfacial kinetics or slow ion transport. Similar to the interdigitated array cell, this advantage is eventually limited by the electronic conductivity of the electrode materials.

It is worth noting that the 3-D interdigitated plate design of Figure 2b can be realized by stacking 2-D

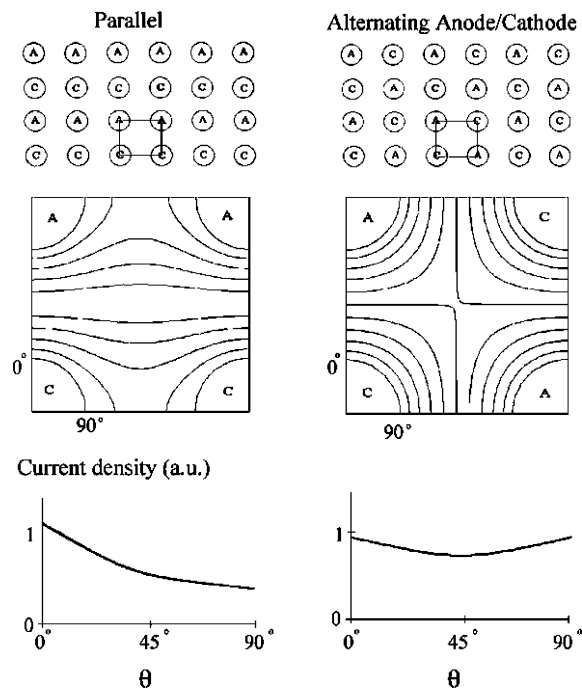


Figure 7. Top panels: Schematic diagram of 3-D cylindrical battery arrays in parallel row (left) and alternating anode/cathode (right) configurations. Middle panels: Isopotential lines between cathode (C) and anode (A) for unit battery cells. Bottom panel: Current densities (in arbitrary units, a.u.) at the electrode surfaces as a function of the angle θ (see middle panel for definition of θ). The area of the cathodes and anodes is equal throughout the diagram. (Reprinted with permission from ref 19. Copyright 2003 Elsevier.)

thin-film batteries. However, to maintain the key advantage of low ohmic potential losses, it is necessary for the thickness of the film electrodes to be greatly reduced. Currently, low-cost manufacturing techniques limit film electrodes to thicknesses greater than about $\sim 20 \mu\text{m}$.

2.3. Current Distribution in 3-D Batteries

2.3.1. Interdigitated Electrode Arrays

All interdigitated electrode arrays suffer from a nonuniform primary current distribution. Figures 7 and 8 show examples of the potential and primary current distributions for representative interdigitated microbattery designs, computed using finite element simulation,²⁵ with the assumption of a uniform electrolyte conductivity. To allow comparison of the current densities between different battery designs, all simulations assume identical values of the voltage between cathode and anode. Current densities are plotted in the same arbitrary units in each figure, allowing direct comparison of the relative power output of different interdigitated geometries. Isopotential lines within the “unit cell” of each interdigitated design are also presented. The lengths of the cathodes and anodes, L , are assumed to be sufficiently long to ignore end effects.¹⁹

Figure 7 illustrates the sensitivity of the current distribution to electrode placement for two similar interdigitated designs. In the parallel row design, alternating rows of cylindrically shaped cathodes and

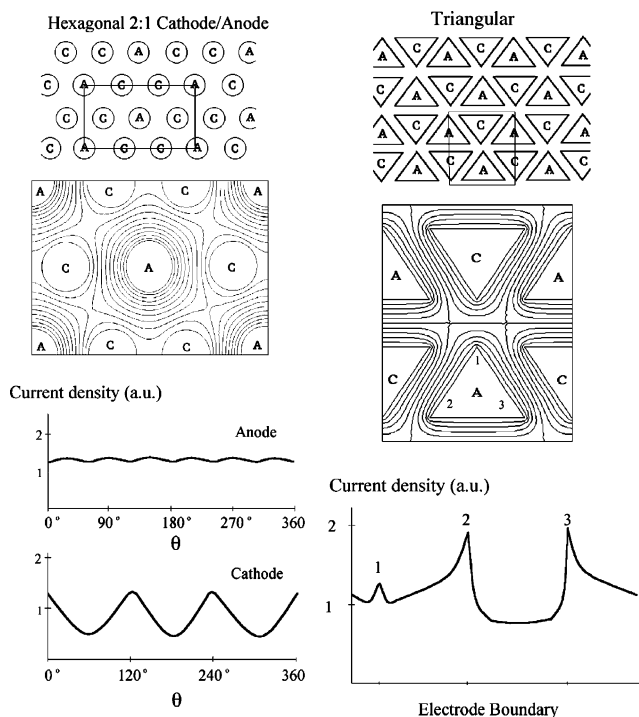


Figure 8. (Top panel, left) Schematic diagram of hexagonal 2:1 cathode/anode battery array. (Top panel, right) Schematic diagram of triangular battery array. (Middle panel) Isopotential lines between cathode (C) and anode (A) for unit battery cell. (Bottom panel) Current density at the cathode and anode surfaces, plotted on the same a.u. scale used in Figure 7. (Reprinted with permission from ref 19. Copyright 2003 Elsevier.)

anodes are placed on a rectangular grid. This arrangement of electrodes results in high current flow between each neighboring cathode/anode pair (i.e., at $\theta = 0^\circ$), with a relatively steep decrease ($\sim 40\%$) in current between adjacent cathodes or anodes ($\theta = 90^\circ$).

A significantly better design based on the rectangular grid is the alternating cathode/anode configuration in which each anode is surrounded by four nearest neighbor cathodes (and vice versa). In this geometry, the higher number of nearest neighbor electrodes of opposite polarity permits a significantly more uniform primary current density at each electrode. However, even in this improved geometry, the current varies by 20% along the electrode circumference, a limitation that may not be tolerable in some cells. The primary current uniformity may be improved by increasing the ratio of the electrode grid spacing to the electrode radius in this cell, but at the sake of reducing power density.

Unlike the conventional battery, a 3-D interdigitated array need not contain equal numbers of anodes and cathodes. Indeed, there may be situations where battery design is optimized by using unequal number densities of cathodes and anodes in order to balance the capacities of the active materials and the kinetics of the charge-transfer reactions. The left-hand side of Figure 8 shows an example of an interdigitated design utilizing twice as many cathodes as anodes. Here, each anode is surrounded by six cathodes, providing a relatively uniform current density on the anode while sacrificing current uniformity at the

cathodes. This design might be useful in a 3-D microbattery where a uniform current density is critical at one electrode (e.g., an insertion electrode).

Modern microlithography allows for the fabrication of essentially any envisioned electrode and cell geometry. Specifically, electrodes need not have the cylindrical shape considered in the previous examples. For example, the close-packed array of triangular cathodes and anodes shown on the right-hand side of Figure 8 would be expected to yield greater cell capacity and increased power. The tradeoff of this design, obviously, is the highly nonuniform primary current. Such a geometry may be appropriate in a situation where the net current is limited by electron-transfer kinetics, and thus the current distribution is uniform across the electrode surface regardless of the electrode geometry.

It is clear that while significant increases in both power and areal energy capacity are obtainable from 3-D interdigitated arrays relative to conventional 2-D batteries, the inherent difficulty in achieving a uniform current distribution may limit some devices. However, interdigitated electrode geometries and configurations not considered above are likely to yield current distributions significantly better than the examples described here.

2.3.2. Plate, Tubule, and Aperiodic 3-D Architectures

The issue of the nonuniform current density is not important for the plate, tubule, and aperiodic architectures shown in Figure 2. The current density in these architectures will be perfectly uniform due to the 1-D nature of transport between anode and cathode. Radial transport occurs in the tubular and aperiodic architecture, while planar transport is operative in the plate architecture (neglecting end effects).

2.4. Overall Design Issues

Modeling the overall current–voltage behavior of 3-D cells is a complex function that depends on many factors (ionic and electronic conductances, interfacial reaction kinetics, charge capacity, etc.). Because of the wide range of possible (and mostly unexplored) architectures, this will be a rich field of study for electrochemical engineers and will likely lead to new design concepts in battery technology. Interdigitated electrode arrays are highly susceptible to stress due to both the nonuniform current density and finite electronic conductivity of the electrodes. Thus, a delicate balance of the geometrical length scales (electrode radius and length, and the spacing between electrodes) and materials properties will be required in optimizing any 3-D battery.

2.5. Cathodes and Anodes Separated by Nanometer-Wide Electrolytes

As noted in section 3.1, the fabrication of cells in which the cathode and anode are separated by a conformal thin-film electrolyte, perhaps a few tens of nanometers in thickness, is on the near horizon. Thus, it is interesting to consider potential phenomena, not normally considered in battery design, that

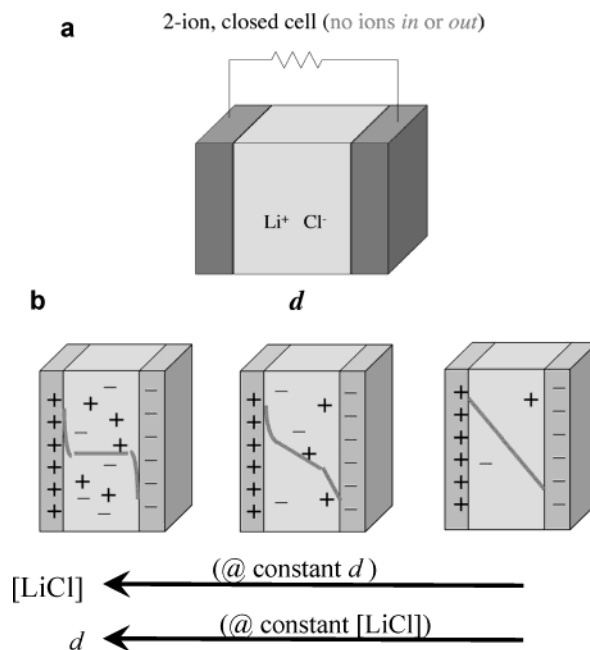


Figure 9. (a) Schematic of a closed cell containing LiCl. The number of ions (Li^+ and Cl^-) is assumed to be constant. (b) The dependence of the potential profile across the two-ion cell as a function of the electrolyte thickness, d , and ion concentration.

will be operative when the electrodes are placed in such close proximity to one another.

For simplicity, we consider a closed cell such as that shown in Figure 9a, which contains LiCl as the electrolyte. Assuming that the cathode and anode are separated by 10 nm (an experimentally achieved separation distance), it is instructive to first consider any direct physical or chemical interactions between the electrodes. Clearly at 10 nm, electron tunneling between the surfaces will be negligibly slow, the decay length of tunneling being ca. 1 Å.²⁶ Thus, the electrodes are not *electronically* coupled, and normal redox reactions at the cathode and anode are still necessary for battery operation. At shorter distances, e.g., 1 nm, the electrodes would spontaneously discharge via direct tunneling between the cathode and anode, a process equivalent to shorting the battery. Thus, there is a theoretical lower limit on the thickness of the battery separator.

Although the cathode and anode are not in electronic communication at 10 nm, their presence is known to each other through the electrical fields that originate from their respective surface charges. As shown in Figure 9b, the overlap of the electrical double layers is more significant as either the distance between the electrodes, d , is reduced or the concentration of the electrolyte is decreased. The role of the electrolyte concentration is quantitatively expressed through the Debye length, κ^{-1} ,²⁶ which can be estimated for a 1:1 electrolyte at room temperature using the expression, κ^{-1} (nm) $\sim 0.3/[\text{LiCl}]^{1/2}$, where $[\text{LiCl}]$ is the molar concentration (M) of the electrolyte. In essence, κ^{-1} represents how well the electrolyte shields the solution interior from the electrical charge of the electrode surfaces. A 1 M LiCl solution corresponds to $\kappa^{-1} = 0.3$ nm, while a 10 mM solution corresponds to a κ^{-1} of 3 nm. As a rule of thumb, the

electric potential drops to about 5% of its surface value at a distance from the surface of $\sim 3\kappa^{-1}$ (i.e., ~ 9 nm in a 10 mM LiCl solution). Thus, two electrodes separated by 10 nm in a 10 mM LiCl solution will clearly be in *electrostatic* contact through their overlapping double layers.

The consequence of overlapping double layers on battery operation has only been recently considered, and our understanding of this effect is rudimentary.²⁴ The electric fields will almost certainly have an effect on the transport of ions through the electrolyte, as migration will be important in the strong fields of the double layers, which can approach or exceed 10^6 V cm⁻¹. Whether transport of Li⁺ is impeded or enhanced by the field will depend on signs of the electrode charges (determined by the potentials of zero charge, an ill-defined quantity for most battery electrode materials) and whether the battery is being charged or discharged. Modeling of this phenomenon requires a simultaneous consideration of transport (e.g., Nernst–Planck equation), electrostatics (Poisson equation), and statistical thermodynamics (Boltzmann equation), similar to recent modeling of the influence of double-layer structure on transport at individual nanometer-scale electrodes²⁷ and Levich's treatment of the dynamic diffuse layer at macroscopic planar electrodes.²⁸

At small electrode separations, the *number* of ions in the electrolyte between the electrodes is quite small. For instance, the average nearest neighbor distance between cations in 10 mM LiCl solution is ~ 2 nm. Thus, on average, only a few Li⁺ ions are located between cathode and anode at any position on the electrode surfaces, and these few ions carry the current at that surface position. The number of ions is so small in this situation that the battery can be well described as a capacitor, with the separator being a nonionic dielectric material, resulting in a linear potential drop between the electrodes (Figure 9b). In addition, even if migration from the electrical double layers is neglected, the small separation distance between the electrodes will result in enormous diffusional fluxes. If sufficiently high, these fluxes can lead to breakdown of electroneutrality and formation of a space-charge layer in the electrolyte.²⁷ Much effort in the future will be required to explore and quantify these ideas.

3. Prior Examples of Small Power

3.1. Scope of Small Power

The development of small power sources for portable electronics goes well beyond miniaturization of batteries and fuel cells.⁴ Other approaches under development include miniaturizing combustion engines and thermoelectrics and harvesting energy from ambient sources such as vibration and temperature differences. Most of these approaches are directed at consumer products and are not designed to save real estate. Nonetheless, it is apparent that decreasing the size of power sources and moving to micro- and even nanoscale power sources offers a number of opportunities.²⁹

Table 1 lists examples of electron-producing power

Table 1. Types of Electron-Producing Power Sources

electrochemical	thermal/nuclear/ mechanical-to-electric
batteries	thermoelectrics
fuel cells, biofuel cells, semi-fuel cells	pyroelectrics
supercapacitors, ultracapacitors	thermionics
photovoltaics	β -cells (nuclear "solar" cells)
harvesting adventitious energy/fuel	harvesting adventitious energy/work
	radioisotope thermoelectric generators (RTGs)— α - or β -emitting nuclear sources

sources, not all of which are electrochemical. The importance of integrating nanotechnology to improve these power sources has been discussed, especially for portable applications.³⁰ Some of these sources are described in greater detail in this section and emphasize those approaches that have demonstrated power production in centimeter dimensions or smaller sizes. The hybrid micropower supplies discussed at the end of this section begin to address the issue of achieving energy and power capabilities in small footprint areas.

3.2. Miniaturizing Microreactors and Fuel Cells

Miniaturization of electrochemical power sources, in particular batteries and fuel cells, has been described as a critical—but missing—component in transitioning from in-lab capability to the freedom of autonomous devices and systems.^{29,30} In top-down approaches, macroscopic power sources are scaled to the microlevel usually by the use of fabrication methods, often in combination with new materials. Power generation schemes that can themselves be microfabricated are particularly appealing, as they can lead to a one-stop fabrication of device/machine function with an integrated power source.

3.2.1. Compact Mixed Reactors

One miniaturization challenge common to fuel cells and batteries—and of critical relevance in designing microscopically and nanoscopically featured 3-D batteries—is scaling down the phase that separates the anode from the cathode. The separator must prevent direct electronic contact yet permit electrical contact (ion flux) between the active electrodes. Electrodes in rechargeable batteries can undergo morphological changes that compromise the integrity of the whole cell, e.g., by establishing a direct electronic path (hard shorts), such as the metal needles that grow off of a charged–discharged zinc electrode and may pierce the separator (glass, polymer, paper) with potentially pyrophoric consequences (one reason the alkaline cell is a primary, use-once, cell).

Fabrication issues can arise when thinning the separator material or in trying to ensure high-quality, preferably pinhole-free coverage of dimensionally scaled-down anodes and cathodes. One strategy that can be used to avoid fabricating a separator at all, at least in electrolyzers and fuel cells, takes advantage of decades of work in compact mixed

reactors (CMR), where the specificity of electrocatalyzed active electrodes permits intermixing of reactants (or fuel/oxidant).³¹ The catalytic specificity bypasses the need for a physical barrier, as long as the electrodes are electronically isolated. Another engineering design feature of these single-chamber systems is the hydrodynamic flow of the molecular reactants.

In 1990, Dyer applied the CMR concept of hydrodynamic control of mixed reactant flow to a thin-film planar fuel cell.³² The electrical (i.e., ionic) contact between the fuel cell anode and cathode was maintained by diffusion across/through a hydrous aluminum oxide film (≤ 50 -nm-thick) sandwiched between the electrocatalytic electrodes, with the top Pt electrode deposited so as to be sufficiently porous for gases to pass through to the alumina membrane. The specific areal power that was generated with a mixed H_2/O_2 flow was $1\text{--}5\text{ mW cm}^{-2}$ at a cell voltage of 950 mV. By using a lightweight substrate (Kapton) onto which the Pt electrodes and hydrous alumina interlayer were deposited as thin films, a power density of 100 W kg^{-1} was reported. Similar results were obtained upon replacing the hydrous alumina membrane with the proton-exchange polymer membrane Nafion, raising the possibility of fabricating conformal, "open-face" fuel cells on a flexible substrate.

3.2.2. Microfabrication Approaches for Small Power

The nickel–zinc battery provides a good example of how macroscopic power sources can be miniaturized via microfabrication methods. A patterned, side-by-side configuration was fabricated with an electroplated zinc anode and a NiOOH cathode (total cell area of 1 to 5 mm^2).³³ A photosensitive epoxy served as the separator and was also used to define the side walls of the cell. The open-circuit voltage of the cells was 1.7–1.8 V. The energy density reported for these Ni–Zn microbatteries (2 J cm^{-2} at 50 mA discharge) is similar to that available with thin-film batteries, although the performance does not achieve the targeted energy density of 1 J mm^{-2} .¹³ The cells do generate reasonable power levels: at a 1 mA discharge rate, the 2-mm^2 cells generate 1–2 mW. As discussed in section 3.5, the Ni–Zn battery is feasible as the energy-storage component in a hybrid micropower system.

Fuel cells incorporating lithographic methods and masking/deposition/etching protocols have been fabricated on Si wafers and thereby satisfy two critical needs in a standard fuel cell: collection of electrons (current collectors) and controlling the flow field of fuel and oxidant.³⁴ Kelley et al. produced a miniature direct methanol fuel cell (DMFC) with a current–voltage and fuel utilization performance that matched standard-sized DMFCs prepared in-lab.^{35,36} A working volume for the miniature DMFC of 12 mm^3 was reported, with an operational performance of 822 W h kg^{-1} at $70\text{ }^\circ\text{C}$.³⁵

In more recent reports, a thin-film fuel cell sandwiched between two silicon wafers that had been anisotropically etched to form feed holes and channels for the reactants (H_2 and O_2) demonstrated a stable voltage of 0.75 V over 300 h at a current

demand of 100 mA cm^{-2} .³⁷ The electrode footprint, which was smaller than the silicon wafers, was $22.5\text{ mm} \times 22.5\text{ mm}$. The same authors have also adapted silicon micromachining to fabricate a twin fuel-cell stack³⁸ using a previously described flip-flop structure sandwiched between silicon wafers again acting as current collectors and flow distributors.³⁴

Wainwright et al. recently microfabricated a polymer-based fuel cell with on-board hydrogen storage. One of the key goals of this work is to provide independent sizing of power and energy capacity in a passive system requiring no fans, pumps, or external humidification.³⁹ The first performance reported was for a device built on a ceramic substrate (alumina), but devices built on silicon and polymeric substrates are also mentioned. The microfabricated fuel-cell block is coupled to a metal–hydride storage block, printed with inks of $\text{LaAl}_{0.3}\text{Ni}_{4.7}$, which generates hydrogen by desorption when placing a 20 mA load on the fuel cell.³⁹

3.2.3. Membraneless Opportunities with Laminar Flow in Microfluidic Reactors

One way to ease any difficulties that may arise in fabricating a membrane, especially in design configurations that are not planar, is to go membraneless. Recent reports take advantage of the laminar flow innate to microfluidic reactors^{40–42} to develop membraneless fuel cells. The potential of the fuel cell is established at the boundary between parallel (channel) flows of the two fluids customarily compartmentalized in the fuel cell as fuel (anolyte) and oxidant (catholyte). Adapting prior redox fuel cell chemistry using a catholyte of $\text{V}^{\text{V}}/\text{V}^{\text{IV}}$ and an anolyte of $\text{V}^{\text{III}}/\text{V}^{\text{II}}$,⁴³ Ferrigno et al. obtained 35 mA cm^{-2} at 1.1 V (for a power density of 38 mW cm^{-2}) at a linear flow rate of 12.5 cm s^{-1} ,^{44,45} which was comparable to that seen with the standard redox fuel cell reported by Kummer and Oei;⁴³ the fuel utilization was, however, much lower. Luo et al. adapted the enzyme-catalyzed redox that powers biofuel cells to create a membraneless microfluidic fuel cell using a molecular fuel (1,4-dihydrobenzoquinone) and a laccase-catalyzed cathode to reduce molecular oxygen. The maximum power density reported was $80\text{ }\mu\text{A cm}^{-2}$ at 150 mV ($8.3\text{ }\mu\text{W cm}^{-2}$) and a linear flow rate of 1 cm s^{-1} , but the cell could sustain 0.35 V at lower current densities.⁴⁶

3.2.4. Power in Vivo and Biologically Derived

One area in which miniaturization has progressed beyond the size regime of interest to the laptop and cellular telephone industry is to provide in vivo power in biomedical applications.⁴⁷ An implantable defibrillator battery, which must provide pulse power (on demand) with high energy density, was achieved by coupling two smaller batteries (Li/MnO_2 primary battery plus a Li/iodine cell) with a packaged volume on the order of 10 mL.⁴⁸ Such power sources must have low self-discharge rates.

In an effort to use biological energy transduction to miniaturize a biofuel cell for in vivo applications, Heller and co-workers have created membraneless, caseless cells that can function under physiological

conditions.^{49–54} The current collectors are microfibers of carbon that are catalyzed with enzymes to oxidize glucose (via glucose oxidase) and reduce O₂ (laccase or bilirubin oxidase) and wired to their respective carbon current collectors with osmium-based redox polymers. The active area of the most recent miniature biofuel cell is 0.44 mm², and this glucose oxidase/laccase-catalyzed biofuel cell produced 0.78 V in a pH 5 buffer at a power density of 2.68 μW mm⁻².⁵³ The improved cell voltage was obtained by using an osmium redox polymer with a more reducing potential, which lowered the overvoltage necessary to drive the coupled enzyme/cofactor redox to convert the glucose fuel to gluconolactone.

Recently a new hybrid power source has been reported that couples oxidation at a dye-photosensitized nanocrystalline semiconducting SnO₂ photoanode with the enzyme-catalyzed reduction of O₂.⁵⁵ Although miniaturization has not yet been reported for this new hybrid, the developments already achieved to miniaturize biofuel cells coupled to those being developed for charge-insertion oxides should be technically transferable to this system.

3.3. Thin-Film Batteries

Miniaturization of batteries has been an active area of industrial research because of the need for portable power sources for such items as watches, hearing aids, and cameras. These miniaturization approaches are based, for the most part, on traditional battery manufacturing, and it is only within the past decade that researchers have begun to employ fabrication methods that rely on more advanced material-processing approaches such as vapor deposition and solution processing. Lithium batteries, in particular, have received considerable attention because of their high energy density. Two complementary lithium batteries have emerged: one is based on polymer electrolytes; the other is based on inorganic electrolytes.¹⁵ The former, which is actually a thick-film system, is the basis for commercial products that provide milliwatt-hour of energy. Primary batteries of the type Li/Li_xMnO₂, marketed by Panasonic among other companies, are on the order of 0.3–0.5-mm-thick and offer between 10 and 20 mA h at 3 V. Secondary (i.e., rechargeable) lithium polymer batteries are also being developed.⁵⁶ The polymer electrolyte in most cases is a gel electrolyte formed by polymers and organic solutions of lithium salts or is a plasticized polymer electrolyte.^{2,57,58}

Inorganic electrolytes lend themselves much more readily to thin-film batteries. Over a decade ago, Eveready Battery developed thin-film Li/TiS₂ secondary batteries, which used a sputtered lithium oxysulfide glass as the electrolyte,⁵⁹ while other thin-film batteries using glassy oxides as the electrolyte continue to be developed.¹⁵ The fact that these inorganic electrolytes have low conductivity at room temperature is compensated by the short diffusion length of only a few micrometers. The fabricated batteries are truly thin film as various vapor deposition methods are used to fabricate the cathode and anode as well as the electrolyte. The total thickness of the active components is in the range of 10–20 μm; however,

the thickness of the actual battery is on the order of 100 μm because of packaging and the critical need to protect the components from moisture.

The thin-film secondary lithium battery system that has progressed the furthest is that developed at the Oak Ridge National Laboratory.¹³ The electrolyte in this case is a lithium phosphorus oxynitride ("Lipon") which is deposited by rf magnetron sputtering, as is the cathode, followed by thermal evaporation of the lithium. A number of different cathode materials, including layered transition metal oxides^{60,61} and vanadium oxides,⁶² have been reported and, for the most part, excellent results have been obtained. The thin-film batteries achieve operating lifetimes of thousands of cycles and routinely operate at current densities above 1 mA cm⁻². In tailoring these batteries for integrated circuit (IC) applications, which involve solder reflow at temperatures of 250 °C, this group developed a lithium-free approach where the anode is formed by electroplating lithium on a copper current collector.⁶³

The research on thin-film batteries has led to considerable understanding of the kinetics and structural changes occurring during lithium insertion and deinsertion in amorphous and nanocrystalline films.¹³ However, the fact remains that these thin-film batteries have limited capacity, because of the thickness of the cathode, while the overall cell resistance can be larger than desired, because of the cathode/electrolyte interface. As a result, cell energies are in the range of 100–500 μW h cm⁻². As discussed previously, these systems are considerably below the 1 J mm⁻² values required for powering MEMS devices.

An interesting direction to thin-film battery fabrication is the use of forward-transfer methods based on laser-assisted direct-write processes. This processing method is a soft transfer that minimally affects the materials being laid down, so it is compatible with the transfer of metals, oxides, polymers, and even liquid and gel electrolytes. The variant known as MAPLE-DW (matrix-assisted pulsed-laser evaporation-direct write)⁶⁴ has recently been used to direct-write a lithium ion battery.⁶⁵ The MAPLE-fabricated LiCoO₂-carbon/carbon microbattery prototype was sealed within trilayer metal-polymer laminate and cycled in air. A typical microbattery with a footprint of 4 mm × 4 mm (patterns can be written to 10 μm) has a capacity of 155 μA h (at a C/5 rate, where a 1 C rate completely discharges the full capacity of the battery in 1 h) and 100 mA h g⁻¹ of LiCoO₂. Because carbon was included in the transfer ink with the charge-insertion oxide, the electrode could be deposited in thicker layers than a sputter-deposited thin-film battery without creating severe ohmic losses. The resulting prototype approaches the power that other thin-film batteries provide but did so with a footprint smaller than 1 cm². An advantage of such direct-write fabrication is that it can ultimately use the electronics substrate as part of the power-source packaging to save weight in the battery system. Current work is aimed at coupling Li ion microbatteries with energy-harvesting devices (solar cells, RF antennae, etc.) for hybrid power supply applications.

Kushida et al. recognized the limitation of the low capacity of thin-film lithium batteries for IC applications when they demonstrated the operation of arrays of thin-film lithium batteries.⁶⁶ Rather than develop a power generator for an entire chip, this work was directed at providing local power to individual (or a few) VLSI circuits. The battery took the form of a 3×1 array in which three parallel $100\text{-}\mu\text{m}$ -wide stripes of cathode material were crossed by a $200\text{-}\mu\text{m}$ -wide stripe of lithium. A spin-on phosphosilicate glass was used as the separator, while the cathode material (LiMn_2O_4) was deposited by solution processing in a trench etched in the silicon wafer to provide better device definition. The prospect of a battery array is an interesting one, and although the energy per unit area was not very high ($\sim 35\ \mu\text{W h cm}^{-2}$), the concept of supplying localized power at the individual circuit level is intriguing.

3.4. Generating Power from Ambient Sources

One important area of MEMS sensor technology is the development of distributed sensors, some of which are embedded, remote sensors in buildings and other structures. Battery replacement is difficult or impractical in this case and approaches for generating power from ambient sources are being pursued. The most familiar ambient energy source is solar and the use of photovoltaics is widely used. Solar energy, however, is not always available for embedded sensors and for this reason another ambient energy source of interest for powering small devices is the use of mechanical vibration. Beeby and co-workers reported the use of an electromagnetic transducer based on the movement of a magnetic pole with respect to a coil.⁶⁷ This electromechanical power generator uses neodymium iron boride permanent magnets mounted on a spring board inside an inductive coil. As the mass deflects from the vibration, there is a varying amount of magnetic flux passing through the coil. An electromotive force is induced (Faraday's law), the magnitude of which is proportional to the rate of change of the coil position. Shaking the device causes the magnets to vibrate at 322 Hz. The device occupies a volume of $240\ \text{mm}^3$ and generated a maximum useful power of 0.53 mW, corresponding to a $25\text{-}\mu\text{m}$ amplitude at an excitation frequency of 322 Hz.

Another power generator that converts vibrational energy to electrical energy is based on a mass-spring-resonator structure.⁶⁸ Laser micromachined copper springs were fabricated into different patterns to optimize device performance. In this device, generators with a volume of $1\ \text{cm}^3$ were able to produce up to 4.4 V peak-to-peak with maximum root-mean-square power of over $800\ \mu\text{W}$. The vibration required to generate this power had frequencies ranging from 60 to 110 Hz with $200\text{-}\mu\text{m}$ amplitude. The fabricated generator was able to drive an infrared transmitter, and the authors contend that the device is capable of driving low-power integrated circuits.

Another approach to converting vibrations in the environment is the use of an inertial generator based on thick-film piezoelectric materials.⁶⁹ A prototype generator was produced enabling the authors to

establish some operating parameters and fabrication methods. For the most part, these methods are expected to provide low power, as the first devices produced an output of 3 mW.

3.5. Hybrid Micropower

In the use of 3-D batteries to power MEMS devices, the tacit assumption is that the battery serves as the electrochemical power source. That is, the battery directly supplies all the energy for the device. A hybrid power supply is an alternative concept based on combining energy conversion and energy storage.¹¹ In this case, the battery is a component of the power supply rather than the sole power source. The batteries are expected to provide power when the energy conversion device is not working or when additional power is required, i.e., pulse power for communication. The energy conversion device, which obtains energy from ambient sources, is used to power the microsystem and charge the batteries.

Koeneman et al. described a micropower supply that was designed to power a "smart bearing".¹¹ The ambient energy, a rotating shaft, was converted using a wire coil. Energy storage was accomplished using a thin-film lithium battery. Because of the device application, a suitable actuation driver was required to deflect the membrane. Although the device was not built, the analysis established that a hybrid power supply could be integrated with a MEMS device to provide on-board power. One interesting point in the analysis is that the authors did not consider the 2-D nature of the battery and overestimated the number of actuations by 50 times.

A more recent paper considered the use of a hybrid power supply for powering autonomous microsensors.⁷⁰ Such devices are similar to the dust mote pictured in Figure 1 and described in the Introduction. This hybrid power supply combined a solar cell to meet standby requirements and to charge the battery, which was the microfabricated Ni-Zn battery described in section 3.2. The authors also showed that if the battery alone was to serve as the power source, the footprint would be substantially larger, over $12\ \text{cm}^2$. The hybrid device was constructed and some feasibility experiments were carried out, but no actual devices were powered.

4. Component Design for 3-D Battery Structures

4.1. Thinking Like Architects

Jumping out of Flatland⁷¹ to a true third dimension (rather than stacking 2-D elements, which seems to be the microlithography community's perception of 3-D) permits the use of hierarchical designs: nanostructured electrode materials, organized into larger macroscopic features. One of the most critical components of these new battery designs is an initial degree of "nothingness", that is a continuous phase of porosity. This open volume is then available to be filled with a second phase, for example an infiltrated electrolyte or even an opposing electrode structure, forming a true 3-D, intermingled battery assembly. Following IUPAC conventions, pores are identified

by their respective sizes: macropores (>50 nm), mesopores (2–50 nm), and micropores (<2 nm).⁷² Nanopore and nanoporous are not internationally defined terms, so they are an unknown and often misleading class of pores.

Chemical methods are ideally suited to construct textured materials with features of solid and void on the meso- or nanoscale. The chemistry can include such techniques as sol–gel synthesis, chemical vapor deposition (CVD), and electrodeposition, where molecular or ionic precursors are reacted under controlled conditions to assemble the desired solid structures. Combining such techniques with structure-directing templates (porous membranes, colloidal crystals, micelles, etc.) permits the design of hierarchical structures with pore sizes that cover a wide range from mesopores to large macropores. In an alternative to template synthesis, sol–gel methods are used to assemble 3-D networks of nanoscale particles into a monolithic wet gel. With careful processing of these gels to remove the pore-filling fluid, aerogels and related structures are rendered that exhibit aperiodic, through-connected void networks of mesopores and/or macropores.

An extensive research effort is currently underway to produce common battery materials, including carbons and transition-metal oxides, in various meso-structured and nanostructured forms. The basic functional requirements for these new materials are largely the same as for conventional secondary battery electrodes: a combination of electrical conductivity and the ability to undergo reversible ion-insertion reactions. However, the inherent characteristics of nanostructured electrode materials, an extensive electrode/electrolyte interface and facile transport of ions through the void volume, yield superior electrochemical performance relative to conventional battery materials. In practically all of the cases discussed below, electrode materials designed with 3-D nanostructured interfaces exhibit significantly better charge-storage properties, particularly under high rates of charge/discharge, than do conventional forms of the same composition, and in some instances, the nanostructured materials provide unexpectedly high overall capacity due to the defective nature of nanoscale solids.

The following section focuses specifically on those design strategies that produce either monoliths or supported films that may then serve as a solid but textured platform in the first design step toward a 3-D battery architecture.

4.2. Porous Membranes as Structure-Directing Templates

The use of porous membranes as templates for electrode structures was pioneered by Martin and co-workers nearly 20 years ago,⁷³ and this approach has since been extended to include numerous electrode compositions and geometries^{73–78} and applications beyond energy storage, including sensing and separations.⁷⁹ In this approach, chemical and electrochemical routes are used to fill in the cylindrical, uniform, unidirectional pores of a free-standing membrane with electrochemically active materials and

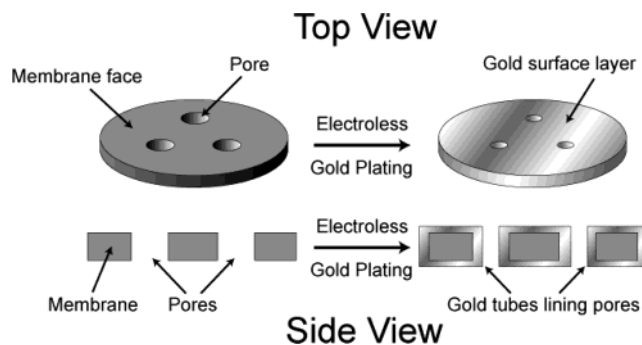


Figure 10. Schematic showing the conversion of a porous membrane into a template in which the pores are filled or coated to form random ensembles or ordered arrays of nanometer- and micrometer-scale cylinders or tubes. (Derived with permission from ref 87. Copyright 1997 Electrochemical Society.)

structures (Figure 10a). The pores in such membranes may be either random, as in “track-etched” polycarbonate, or an ordered array, as in electrochemically prepared alumina membranes. The pores in these membranes can be as small as 10 nm and range upward into the hundreds of nanometers and micrometers.

Various strategies are used to produce electrode structures within the membrane pores, including sol–gel synthesis, CVD, electrodeposition, and electroless deposition. With careful control of the synthetic conditions, the pores are either filled completely or preferentially coated at the pore walls, producing hollow tubes (see Figure 10b). Following infiltration with the desired electrode material, the membrane is subsequently removed under conditions that do not disturb the active material, leaving an array of either solid nanofibers or nanotubes attached to a current collector like the bristles of a brush (Figure 11). In this case there is very limited interconnectedness between the nanofibers, except at the current collector base.

Using this approach, template-synthesized electrodes have been prepared not only from metals, but from TiO_2 ,⁷⁵ V_2O_5 ,^{80,81} LiMn_2O_4 ,^{82,83} SnO_2 ,^{84–86} TiS_2 ,⁸⁷ carbon,^{88–90} and various conducting polymers.⁹¹ The final templated feature need not consist of a single material or phase. Martin and co-workers prepared striped metal nanorods of gold and platinum,⁹² which was a concept ultimately extended to the preparation of nanoscopic barcodes⁹³ and optical tags.⁹⁴ Recently Dewan and Teeters infiltrated alumina membranes to template a device: a V_2O_5 xerogel–carbon battery using a poly(ethylene oxide)–lithium triflate electrolyte.⁹⁵

Many of the templated electrode ensembles described above function as high-performance battery electrodes in lithium-containing electrolytes.⁷⁶ The fibrous morphology of these templated electrodes reduces the solid-state transport distances for lithium ions participating in the charge-storage reaction. This feature facilitates not only good cyclability but also rapid charging and discharging. For example, template-synthesized SnO_2 electrodes deliver gravimetric capacities that are orders of magnitude higher than a thin-film control electrode when discharged at greater than a 50 C rate. The void spaces between

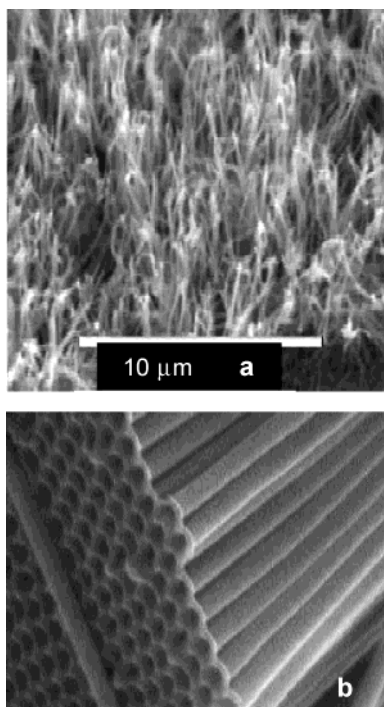


Figure 11. Electron micrographs of membrane-templated electrodes: (a) ensemble of rods (Reprinted with permission from ref 80. Copyright 1999 Electrochemical Society.); (b) array of nanotubes (Reprinted with permission from ref 79. Copyright 2001 American Chemical Society.)

the individual electrode fibers also provide room for expansion during electrode cycling, which is a particular problem for SnO_2 , because a Sn metal phase alloys with electrogenerated Li metal, with accompanying large volume changes.

In a related approach, these same porous alumina membranes serve as a mask through which O_2 plasmas are used to etch underlying carbon films.^{96,97} This etching process produces honeycomb carbon structures that are positive replicas of the alumina-membrane mask. This process has successfully produced honeycomb structures of both diamond⁹⁶ and graphitic carbon,⁹⁷ with pore sizes in the carbon replica around 70 nm.

4.3. Template Synthesis of Ordered Macroporous Solids with Colloidal Crystals

The porous membrane templates described above do exhibit three-dimensionality, but with limited interconnectedness between the discrete tubelike structures. Porous structures with more integrated pore–solid architectures can be designed using templates assembled from discrete solid objects or supramolecular structures. One class of such structures are three-dimensionally ordered macroporous (or 3-DOM) solids,⁹⁸ which are a class of inverse opal structures.⁹⁹ The design of 3-DOM structures is based on the initial formation of a colloidal crystal composed of monodisperse polymer or silica spheres assembled in a close-packed arrangement. The interconnected void spaces of the template, ~ 26 vol % for a face-centered-cubic array, are subsequently infiltrated with the desired material.

Strategies for filling the void space of the colloidal crystal utilize sol–gel chemistry, salt precipitation,

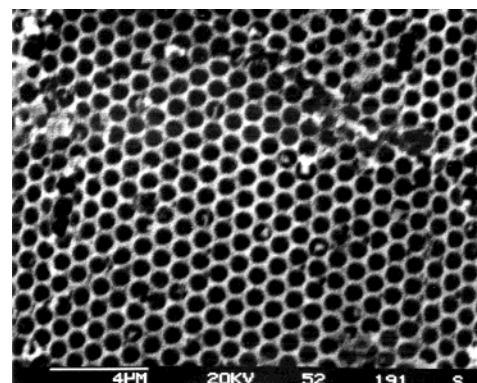


Figure 12. Inverse opal of vanadium oxide ambigel. The pores are formed by packing 1- μm styrene beads and infiltrating a vanadium sol. (Reproduced with permission from ref 100. Copyright 2002 The Royal Society of Chemistry.)

CVD, and electrodeposition, depending on the desired composition. Removal of the colloidal templating spheres renders a negative replica (the inverse opal) structure of the active material, with an interconnected, 3-D array of pores, typically sized in the hundreds of nanometers.

This general procedure for producing macroporous solids has recently been exploited to synthesize electrode architectures that are targeted for lithium battery applications. Sakamoto and Dunn synthesized inverted opal structures of V_2O_5 by infiltrating a colloidal crystal template with a vanadia sol–gel formulation.¹⁰⁰ The resulting macroporous structure is shown in Figure 12. The walls are composed of vanadium oxide ambigel, leading to a hierarchical architecture that demonstrated high capacity for lithium at high discharge rates. Stein and co-workers have expanded this concept further to produce macroporous ordered structures of V_2O_5 , SnO_2 , and LiNiO_2 .^{98,101} Hierarchical electrode structures are generated by this method as well, with the inorganic skeleton of the 3-D ordered macroporous structure composed of fused nanoscale grains of electrode material that are themselves mesoporous. Macroporous carbon structures have also been produced by infiltrating organic precursors into the interstitial void of silica sphere colloidal crystals, followed by carbonization and removal of the silica template.^{102–106}

4.4. Template Synthesis of Mesoporous Solids with Supramolecular Assemblies

These same general templating strategies are extended into the mesopore size regime with the use of self-assembled supramolecular arrays, a topic which has been extensively reviewed elsewhere.^{107–121} In this approach, ionic surfactants or block copolymers are assembled into micellar aggregates or liquid-crystalline phases. With careful tuning of the reaction conditions, these assemblies can be organized into either highly ordered hexagonal, lamellar, or cubic structures, or more disordered wormlike structures. The microscale phase segregation in these systems acts to restrict and direct the growth of an inorganic guest phase, which can be incorporated by various methods. With transcriptive synthesis the

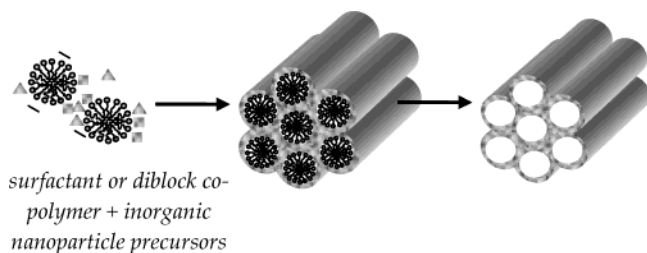


Figure 13. Self-assembled organic template (micellar or liquid crystalline) that directs the assembly of the inorganic phase about the structure-directing organic phase. (Courtesy of Prof. Sarah Tolbert, UCLA.)

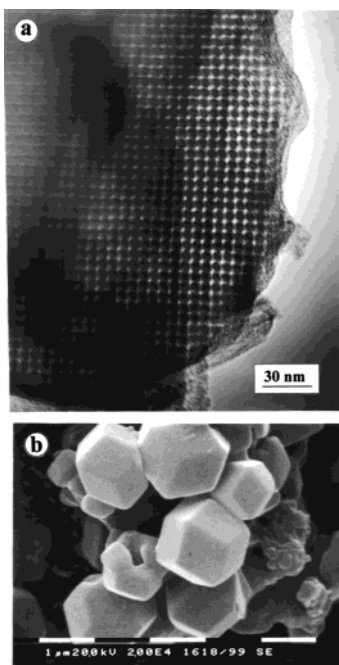


Figure 14. Nanocast carbon. (Reprinted with permission from ref 122. Copyright 1999 American Chemical Society.)

supramolecular assembly is first formed separately followed by infiltration of the guest phase. Synergistic synthesis encompasses the process whereby template self-assembly and inorganic phase synthesis are combined in a cooperative reaction scheme to produce the mesostructured hybrid (Figure 13).

In either the transcriptive or synergistic strategy, removal of the organic template by extraction or calcination renders the inorganic mesoporous structure. For synthetic schemes that are not compatible with the formation of stable template assemblies, an alternative approach is to use a preformed, templated inorganic host, such as mesoporous silica, as a mold to “nanocast” the desired material as an inverse replica of the host, such as that seen in Figure 14.¹²²

In the following section, we restrict our discussion to templated mesoporous solids that are of potential interest as battery electrodes, including many transition-metal oxides and carbon. This slice of the literature still points the interested reader to many articles on the synthesis and physical characterization of relevant mesoporous materials. A much smaller number of electrochemical studies with templated mesoporous electrodes have been published, and these studies in particular will be noted.

The synergistic synthesis method for supramolecular templating was initially developed for silica solids, but this chemistry is being expanded to include a number of transition-metal oxides, including some of interest for electrochemical applications.^{112,123} Among these, mesoporous TiO_2 has been the most widely investigated, primarily due to its potential employment in photovoltaic cells.¹²⁴ Combining liquid-phase titania precursor chemistry and templating strategies has produced mesoporous TiO_2 structures, with both ordered and wormlike pore structures.^{125–133} Grätzel and co-workers have reported on the reversible lithium ion insertion reactions of mesoporous anatase TiO_2 .^{127,134,135} Similar strategies have been used to generate mesoporous WO_3 , an important electrochromic oxide, where the high surface areas and mesoporous pathways facilitate rapid coloration/decoloration responses.^{136,137}

Another route to mesoporous, electrochemically active phases utilizes electrodeposition methods, where the presence of surfactants or a liquid-crystalline phase at the electrode surface directs the formation of the growing film. The templated electrodeposition approach was initially developed by Attard et al. to produce mesoporous platinum films.¹³⁸ This protocol was followed to develop mesoporous tin as a potential anode for Li ion batteries and nickel/nickel oxide electrodes for aqueous-based batteries.^{139,140} Related strategies have also been used to prepare mesoporous V_2O_5 ¹⁴¹ and conducting polyaniline (as nanowire arrays).¹⁴² In addition to driving the electrodeposition process, the electrochemical interface can be controlled to promote the formation of hybrid assemblies of surfactant–inorganic in dilute surfactant solutions en route to forming mesoporous oxide films, as demonstrated by Stucky et al.^{143,144}

Templated mesoporous carbon structures are generally produced by first incorporating organic precursors into the void space of a preformed mesoporous silica or aluminosilicate template, either by liquid infiltration or CVD methods. Following pyrolysis of organic components, the inorganic templates are removed, rendering an inverse carbon replica. This approach was first reported by Ryoo and co-workers¹²² and has subsequently been extensively adapted to generate various mesoporous carbon structures.^{104,145–161} The pore–solid architectures of these carbon solids can be designed on the basis of the choice of inorganic template from among the many available and range from ordered 2-D structures to more disordered 3-D structures. These mesoporous carbons are promising candidates as electrochemical materials in double-layer capacitors. The mesoporous pathways within these electrode structures promote rapid transport of electrolyte ions during cycling, resulting in electrodes that can be charged and discharged rapidly with only minimal loss of capacity.^{150,162–164}

4.5. Hierarchical Designs Based on Templating Strategies

Hierarchical structures with pore–solid features that cover a wide size range within one structure, as seen in Figure 15, are achieved by carefully combin-

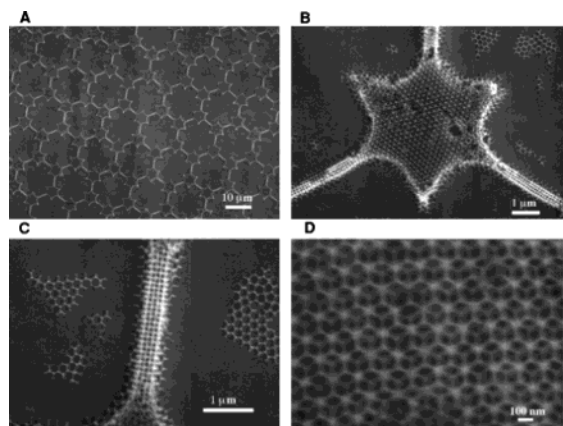


Figure 15. Hierarchical structure formed by combining liquid-phase templating with micromolding. (Reprinted with permission from ref 166. Copyright 1998 American Association for the Advancement of Science.)

ing the liquid-phase templating approaches described above: surfactant templating (up to 10 nm), block copolymer templating (up to 30 nm), and colloidal crystal templating (100 nm–1 μm).^{165,166} This strategy can be used directly to fabricate inorganic structures or indirectly for hierarchical, porous carbon structures that are produced by inverse replication of a corresponding hierarchical inorganic mold.¹⁶¹ These synthetic processes can be further combined with micromolding techniques to create features up to 1 mm.¹⁶⁶

4.6. Aerogels and Related Nanostructures—Aperiodic Pore–Solid Architectures

An ordered porous network is not a prerequisite in designing high-performance 3-D battery structures.¹⁶⁷ Sol–gel methods can be used to synthesize monolithic gels that are composed of a 3-D interconnected network of nanoscale particles, co-continuously intermingled with a phase of fluid-filled pores. The processing of these wet gels to render the dried forms must be carefully controlled so that the highly porous architecture is retained. The direct evaporation of typical pore-filling fluids (high-surface-tension liquids such as water and alcohols) creates capillary forces at the liquid–vapor interface, resulting in pore collapse and a partially densified porous solid known as a xerogel. This structural collapse is avoided if the pore fluid is removed under supercritical conditions where no liquid–vapor interface is ever established. Gels processed by supercritical fluid extraction, usually with CO_2 as the pore fluid, are denoted as aerogels.^{167–170}

In an alternative to supercritical drying, the pore fluids in a wet gel are replaced with a low-surface-tension, nonpolar liquid, such as an alkane, which is then allowed to evaporate under subcritical or ambient-pressure conditions.^{170–172} The resulting solids, denoted as “ambigels” (for ambient-pressure-dried gels),¹⁶⁷ do exhibit a moderate degree of densification but retain a large fraction of pore volume, with pores usually in the mesopore size range.^{173–175} The densification that accompanies ambient-pressure drying provides for more mechanically rugged monolithic

forms than those for comparable aerogels. A fourth scheme of pore-fluid removal utilizes a freeze-drying process to render highly porous “cryogels”.^{176–180}

Aerogels and related structures have the important characteristics of extremely high surface area and a through-connected, aperiodic network of porosity. Additionally, these solids can be cast and molded into a range of shapes and forms or cast as thin films on planar supports. One attribute that seems to set these aperiodic architectures apart from the mesoporous ordered solids, even the nominally 3-D porous ones, is proven performance in rate-critical applications. The rapid and facile flux of molecules through the aerogel architecture avoids the potentially devastating loss of throughput through 1-D channels if a blockage occurs.¹⁸¹ Aerogels have already demonstrated orders of magnitude faster response for sensing, energy storage, and energy conversion than other pore–solid architectures.^{167,181}

Electrically conductive aerogels have been prepared from a range of transition metal oxides, including vanadium oxide,^{172,182–189} manganese oxide,^{173,174,190} molybdenum oxide,^{191–193} and tin oxide.¹⁹⁴ All of these nanostructured oxide forms exhibit improved performance as Li ion insertion electrodes in conventional electrochemical cells.^{167,195} For example, vanadium pentoxide aerogel electrodes accommodate the reversible electrochemical insertion of up to four Li ions per V_2O_5 unit. In addition to higher overall capacities, aerogel electrodes deliver more energy (capacity) under high charge–discharge rates than do conventional materials.

Carbon aerogels are typically derived from the reaction of resorcinol (or related aryl precursors) and formaldehyde, which leads to a polymer gel. The postprocessed polymeric aerogels are then pyrolyzed in inert atmospheres at high temperature to form highly conductive, monolithic carbon structures that retain the characteristics of an aerogel.^{196–198} The synthesis of carbon aerogels offers considerable flexibility as the pore–solid organic architecture can be adjusted by simple changes in the initial reaction conditions of the polymer gel. Through such variations, carbon aerogels can be prepared in either predominantly mesoporous or macroporous forms. Carbon aerogels are being exploited as electrodes for electrochemical capacitors, where the high surface area, through-connected porosity, and electronic conductivity of the aerogel promote rapid charge–discharge reactions.^{199–201} Commercial supercapacitors based on carbon aerogels are available from several companies.

5. Structural Characterization of 3-D Electrode Architectures

5.1. Characterization of the Pore–Solid Architecture

The common feature of the 3-D electrode structures described above is the intimate intermingling of solid and void space, in either ordered or aperiodic arrangements, with textures covering an extensive range of length scales. This section reviews the experimental methods used to characterize the pore

size and structure and to determine the electrochemical properties of the pore–solid nanoarchitectures. The quality and type of pore structure in such an architecture often determines the electrochemical performance of the resulting battery material. For instance, when the pore structure is infiltrated with a liquid electrolyte, interconnected mesopores and macropores provide an open pathway for the diffusion of electrolyte ions that participate in the charge-storage mechanisms. The size and interconnectedness of the pore network will be crucial in achieving true intermingled cathode/electrolyte/anode designs.

From the standpoint of electrochemical performance, micropores (less than 2 nm) are a far less desirable design component for 3-D power. Even when employed in traditional electrochemical cells, the electrode area within a micropore is not fully utilized in energy-storage mechanisms, due to the lower effective electrolyte conductivity within the micropore and sieving effects for larger electrolyte ions.^{202,203} Although templated microporous materials, especially in carbon, have been fabricated and characterized for catalytic and adsorbent applications, we are not including this class of materials for further 3-D design consideration because of the inability to electrify the surface area within micropores on a practical time scale.

5.1.1. Physisorption

Gas adsorption techniques are often used to characterize the pore structure of materials possessing micropores, mesopores, and small macropores.²⁰⁴ Adsorption measurements with probes such as N_2 provide information on accessible surface area and pore volume. In addition, careful analysis of the experimental data also yields information about pore sizes, shapes, and the degree of interconnectedness.²⁰⁵ Various mathematical models can be used to fit the experimental data from adsorption isotherms, yielding pore–size distribution (PSD) plots describing the pore structure in the mesopore and small macropore regime. The generation of PSD plots is critical in the characterization of structured materials with aperiodic pore–solid architectures, such as aerogels and ambigels, where it is difficult to directly image the pore structure with microscopic techniques. In Figure 16, the pore–size distributions are contrasted for birnessite, a Na^+ -templated, sol–gel-derived lamellar polymorph of MnO_2 , expressed in three types of pore–solid nanoarchitectures (xerogel, ambigel, and aerogel). The PSD plots make it clear that the pore structure in xerogels comprises micropores and small mesopores, while the distribution in the aerogel is weighted toward the larger mesopores and macropores. The ambigel lives up to its name with few micropores and macropores and most of its pore volume represented in mesopores sized from 15 to 30 nm.¹⁷⁵ Reporting just the average pore diameter does not begin to capture the richness of the nanoarchitectures: xerogel, 9 nm; ambigel (hexane), 12 nm; ambigel (cyclohexane), 17 nm; and aerogel, 19 nm.

5.1.2. Small-Angle Scattering Techniques

A second approach to pore–structure analysis, small-angle scattering (SAS), probes the heteroge-

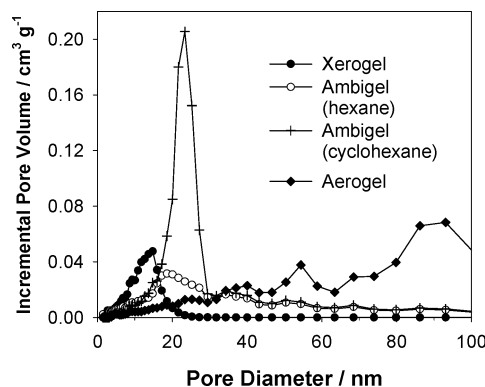


Figure 16. The pore-size distribution for sol–gel-derived birnessite $Na_3MnO_2 \cdot xH_2O$ as processed into three pore–solid nanoarchitectures: xerogel, ambigel, and aerogel. Distributions are derived from N_2 physisorption measurements and calculated on the basis of a cylindrical pore model. (Reprinted with permission from ref 175. Copyright 2001 American Chemical Society.)

neities in electron density within porous architectures.^{204,206} Small-angle scattering measurements extend the range of length scales that can be analyzed, revealing features from micropores to the large macropores that cannot be effectively probed by gas adsorption. Another distinguishing feature of SAS techniques is that both open and isolated pores contribute to the experimentally observed structure. The results of gas adsorption analysis and such SAS techniques as small-angle X-ray scattering (SAXS) can be combined to provide the most thorough characterization of complex pore–solid architectures. A key recent advancement for SAS methods has been the development of the chord-length distribution (CLD) approach, which yields much more accurate characterizations of pore sizes and distributions than with previous SAS approaches.^{207,208}

5.1.3. Electron Microscopy

Electron microscopy techniques are routinely applied to structured nanomaterials to assess the solid morphology for features from tens of micrometers to nanometers in size. Traditional microscopy methods provide useful information in the form of 2-D projection images, but they do not fully describe the 3-D structures discussed in the preceding section. However, the recent advancements in computer-aided electron microscopy techniques do provide 3-D information for structured solids.^{209–212} One such approach based on high-resolution electron microscopy (HREM) was developed by Terasaki, Stucky, Ryoo and others specifically for porous structures exhibiting long-range periodicity on the mesoscale (i.e., templated mesoporous solids).^{212–216} In this method, 2-D projected HREM images of the sample taken at different symmetry orientations are subjected to Fourier transform analysis to determine the crystal structure factors and ultimately to obtain a 3-D representation of the ordered structure. The measurements provide information on the sizes, shapes, and connectivity of the ordered pore structures in such materials as templated mesoporous silica and carbon (see Figure 17). Unfortunately, these methods are not applicable

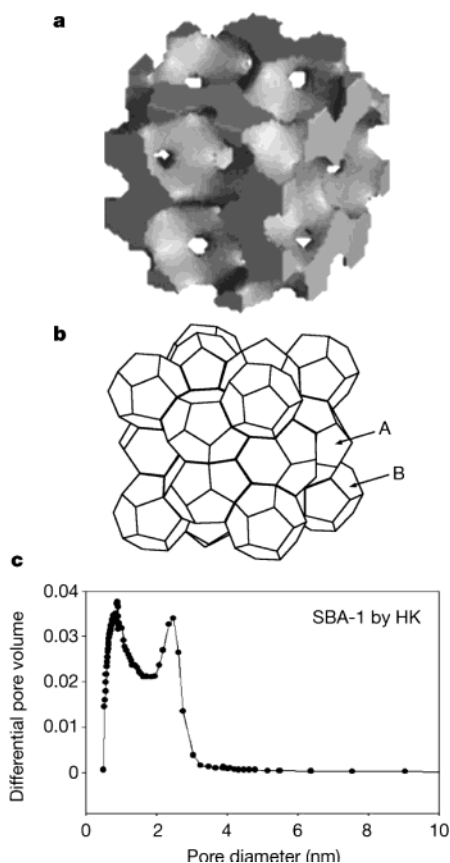


Figure 17. High-resolution electron micrographic determination of cage and bimodal pore structure in the mesoporous silicates SBA-6 and SBA-6: (a) 3-D structure of SBA-6 derived from the electrostatic potential map showing large (A) and small (B) cages with associated large and small pores; (b) schematic of the large and small cages in the SBA family; (c) pore sizes for calcined SBA-1 determined by Horvath–Kawazoe analysis of the argon adsorption isotherm branch. (Reprinted with permission from ref 213. Copyright 2000 Macmillan Magazines, Ltd.)

for materials with irregular or hierarchical pore–solid architectures.

A more general approach to 3-D structure determination is electron tomography, where the 3-D image of a solid (in a thin slice) is reconstructed from a series of 2-D images taken at regular tilt angle intervals.²⁰⁹ Although not yet a common technique for materials science, electron tomography is emerging as a powerful tool for imaging complex solids with features approaching the nanometer scale.²¹⁷ This technique is also more generally applicable to the textured materials described in this review, as it does not rely on any long-range order within the sample.

In addition to providing insights into sample morphology, electron tomography can also be exploited to derive 3-D compositional information. For instance, energy-filtered transmission electron microscopy (EFTEM) or Z-contrast scanning transmission electron microscopy (STEM) can be combined with tomography to provide 3-D elemental mapping capabilities, within some limitations, for light and heavy elements, respectively.²⁰⁹ In the future, electron tomography will be highly beneficial for characterizing the multifunctional architectures that are currently being designed for 3-D power sources.

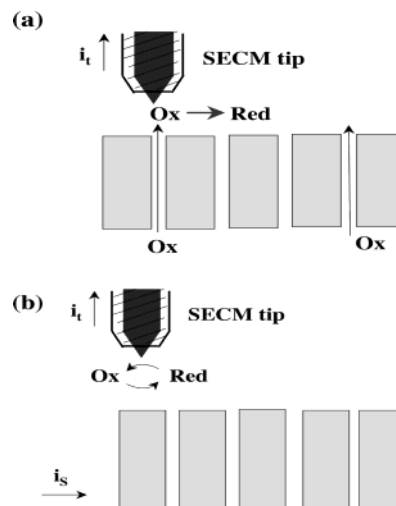


Figure 18. Schematic drawing depicting SECM measurement of (a) molecular transport within a porous material and (b) electrochemical activity on one electrode in a battery array.

5.1.4. Scanning Probe Microscopy

Scanned probe microscopies (SPM) that are capable of measuring either current or electrical potential are promising for in situ characterization of nanoscale energy storage cells. Mass transfer, electrical conductivity, and the electrochemical activity of anode and cathode materials can be directly quantified by these techniques. Two examples of this class of SPM are scanning electrochemical microscopy (SECM) and current-sensing atomic force microscopy (CAFM), both of which are commercially available.

In the SECM measurement (Figure 18), a small microelectrode (typically a metal or carbon electrode) is rastered across the surface of interest, and the current resulting from a Faradaic reaction is measured.^{218–220} The experiment is arranged such that the tip current is proportional to the local concentration of a redox species, which in turn may reflect molecular transport rates within a porous matrix (Figure 18a)²²¹ or the electron-transfer activity at an electrode (Figure 18b).

Quantitative theories of various SECM experiments are well-developed and have been applied in investigations of both electrochemical and nonelectrochemical systems,²²² including, for example, investigations of electro-osmotic flow and transport rates in fuel-cell membranes.²²³ Because one detects molecules that are undergoing random diffusion, the spatial resolution of SECM is not as great as that of scanning tunneling microscopy. However, the nanoscale pore structure in Nafion membranes has been imaged by this technique, demonstrating better than 5-nm spatial resolution.²²⁴ And in contrast to STM or AFM, the SECM signal is very specific to local chemistry, providing a wealth of information about local concentrations of ions and molecules, chemical kinetics, and transport rates.

A complementary microscopy to SECM is CAFM, in which the AFM tip is made of a metal such that current can be measured as the tip is scanned, in contact, across the surface.²²⁵ Conducting-AFM offers the advantage of directly measuring local electrical

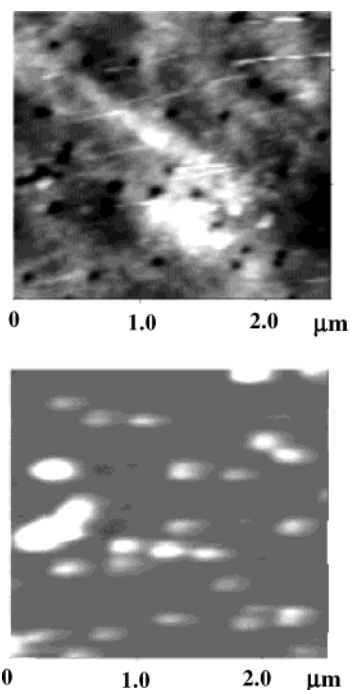


Figure 19. SECM–AFM images of a polycarbonate membrane containing 100-nm-radius pores. (Top) AFM topography image; (Bottom) SECM image of $\text{Ru}(\text{NH}_3)_6^{3+}$ transport in membrane pores. (Reprinted with permission from ref 227. Copyright 2001 American Chemical Society.)

conductivity, which can be inferred only from the SECM measurement. More importantly, both topography and surface electronic conductivity can be measured simultaneously, allowing the experimentalist to correlate structure and reactivity. An example of this is the CAFM imaging of electronic defects in the native oxide on titanium electrodes, which shows that high conductivity is associated with grain boundaries of the underlying metal.²⁵ Additional CAFM studies have focused on the investigation of the electrical properties of electrocatalytic Pt nanoparticles deposited on and in a porous Ti/TiO₂ film.²²⁶

A recent development in SPM technology is the combination of SECM and AFM to produce a hybrid high-resolution microscope that allows simultaneous topographic and electrochemical imaging.²²⁷ Figure 19 shows an example of this measurement in which pore structure and molecular transport of a redox-active molecule ($\text{Ru}(\text{NH}_3)_6^{3+}$) were simultaneously imaged at ~ 1 -nm resolution. Inspection of this image clearly shows a correlation between transport rates and pore structure.

Potential applications of SECM and CAFM in fundamental studies of nanoscale batteries and battery materials are readily envisioned. For instance, a small ion-selective electrode can be used as the SECM tip, providing a means to image and quantify Li^+ distribution and transport rates. A second application is mapping the electrostatic potential distribution between cathode and anode using a well-poised reference electrode as the scanning tip. Conducting-AFM imaging of battery electrode matrices comprising electronically insulating electrolyte and a conducting material would allow rapid visualization of electrical connectivity.

5.2. Corroboration of Electrochemical Processes with Spectroscopic Techniques

Three-dimensional electrode nanoarchitectures exhibit unique structural features, in the guise of amplified surface area and the extensive intermingling of electrode and electrolyte phases over small length scales. The physical consequences of this type of electrode architecture have already been discussed,¹⁶⁷ and the key components include (i) minimized solid-state transport distances; (ii) effective mass transport of necessary electroreactants to the large surface-to-volume electrode; and (iii) magnified surface—and surface defect—character of the electrochemical behavior. This new terrain demands a more deliberate evaluation of the electrochemical properties inherent therein.

Many of the traditional electroanalytical methods can be coupled to spectroscopic measurements, either ex situ or in situ, to elucidate the electronic and structural changes that accompany the electrochemical charge-storage process. The simplest approach takes advantage of the electrochromic properties of the various transition-metal oxides and the changes that occur upon charge insertion and de-insertion. The electrochromic response of thin oxide films supported on conductive, transparent substrates provides an in situ, temporal indicator of electronic state changes that occur during ion-insertion reactions. The power of spectroelectrochemistry arises from the fact that the spectral information, obtained concurrently with the electrochemically driven electronic state changes, decouples from other electrochemical phenomena, such as double-layer capacitance and electrolyte decomposition, which can potentially interfere with the electrochemical-only characterization.²²⁸

Spectroelectrochemical analysis of charge-insertion nanostructured materials already offers important insight into these systems. These methods were recently exploited to characterize the electrochemical processes of nanostructured manganese oxide ambigel and xerogel films.^{175,229} Spectroelectrochemical measurements were used to corroborate electronic state changes with the observed electrochemical response for the insertion of small cations (Li^+ , Mg^{2+}) and the unexpected insertion of a bulky organic cation (tetrabutylammonium). Vanadium pentoxide exhibits two distinct electrochromic features that can be assigned to the $\text{V}^{\text{V}}/\text{V}^{\text{IV}}$ transition at either stoichiometric V_2O_5 sites or V sites adjacent to oxygen vacancy defects.²³⁰ Exploiting this phenomenon, Rhodes et al. were able to assign these different physical environments in the voltammetry for sol-gel-derived V_2O_5 (Figure 20) and to track the relative distributions of these two energetically distinct insertion sites for sol-gel-derived V_2O_5 films as a function of temperature–atmosphere treatments.^{231,232}

For more sophisticated spectroelectrochemical analysis, electrochemical cycling is coupled with X-ray absorption spectroscopy (XAS) methods, which probe electronic and local atomic structures with element specificity.^{233,234} Because XAS techniques are compatible with in situ investigations and do not require long-range structural order for analysis, they are

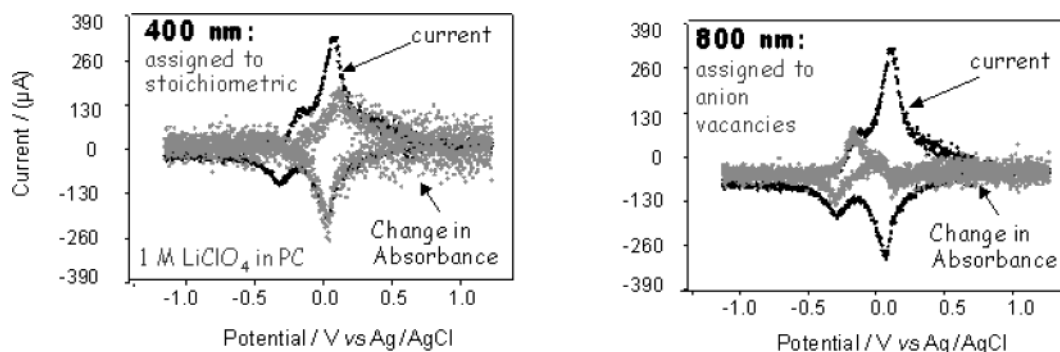


Figure 20. Spectroelectrochemical analysis of thin films of V_2O_5 ambigels supported on conductive glass (indium–tin oxide). The current response is given by the continuous line, and the change in absorbance monitored at 400 and 800 nm as a function of potential (and time) is shown as individual data points. The V_2O_5 ambigel was prepared by gelation of aqueous metavanadate, dried from cyclohexane, and calcined in air at 170 °C. (Printed with permission from ref 232.)

often used to characterize complex battery materials as a function of electrochemical state.^{235–239} Sol–gel-derived V_2O_5 electrodes are prime candidates for XAS analysis due to their disordered, nanoscale nature and exceptional electrochemical properties.^{240–245} As noted earlier, V_2O_5 ambigels and aerogels exhibit anomalously high capacities for Li ion insertion, with insertion of up to four Li per V_2O_5 for electrochemical lithiation and up to six Li per V_2O_5 with chemical lithiation.²⁴⁵ On the basis of the conventional insertion mechanisms, any lithiation beyond $x = 2$ for the formula $Li_xV_2O_5$ should result in the formation of V^{III} sites in the oxide lattice. Passerini et al. reported that for chemically lithiated V_2O_5 , the formal vanadium oxidation state unexpectedly did not go below the V^{IV} state, even with lithiation up to $Li_{5.8}V_2O_5$, suggesting charge delocalization beyond the V sites.²⁴⁵ But Mansour et al. recently described in situ XAS analysis of V_2O_5 aerogels and ambigels, demonstrating that with electrochemical cycling the high degree of Li ion insertion is accompanied by the formation of V^{IV} and subsequently V^{III} sites, when the degree of lithiation surpasses two Li per V_2O_5 .^{243,244}

One concern that might arise in using electronic spectroscopy to quantify highly defective structures is hinted at by results with nanostructured birnessite $Na_0MnO_2 \cdot xH_2O$. The color center in MnO_2 is the Mn^{4+} center, so optical density is lost in the visible spectrum as $Mn(III)$ sites are electrogenerated (see Figure 21). The as-prepared and calcined birnessite ambigel is mixed valent but predominantly $Mn(IV)$, which can be quantitatively assayed by chemical redox titration.^{174,175} The initial visible spectrum, which measures the electronic state of the Mn centers, has a lower absorbance than the material after electro-oxidation, in agreement with the chemically determined mixed-valence state of the initial material. The spectrochemical determination of the $Mn(III)/Mn(IV)$ ratio, however, does not match that obtained by chemical titration and undercounts the amount of $Mn(IV)$. Because of the high surface-to-volume ratio and greater defect nature of these nanostructured materials, we question whether any spectroscopic electronic state measurement truly measures a localized site that remains unaffected by the vacancies that arise in these materials.

Characterizing (experimentally and computationally) and exploiting the nature of defects in charge-

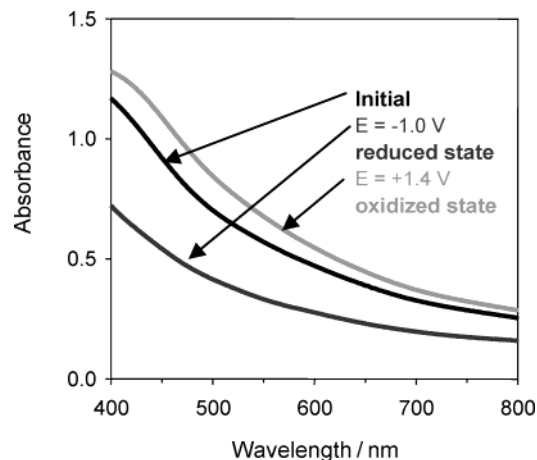


Figure 21. Visible absorption spectra for a 1.6- μm -thick $Na_0MnO_2 \cdot xH_2O$ birnessite ambigel film in 1 M $LiClO_4$ /propylene carbonate as a function of electrode potential. (Reprinted with permission from ref 175. Copyright 2001 American Chemical Society.)

storage materials is a key area of future research in the drive to improve the performance of batteries and ultracapacitors.¹⁶⁷ As discussed above, the aerogel forms of disordered $V_2O_5 \cdot 0.5H_2O$ afford Li-to- V_2O_5 stoichiometries of 4–6,^{183,195} while those for the bulk, crystalline material are 1–2.²⁴⁶ One clue to this impressive improvement in the Li ion capacity of V_2O_5 can be found by inducing deliberate defects in polycrystalline V_2O_5 :²⁴⁷ Creation of proton-stabilized cation-vacancies increases the capacity 23% relative to the $\sim 170 \text{ mA h g}^{-1}$ obtained with the as-received, micrometer-sized polycrystalline V_2O_5 .

While XAS techniques focus on direct characterizations of the host electrode structure, nuclear magnetic resonance (NMR) spectroscopy is used to probe local chemical environments via the interactions of insertion cations that are NMR-active nuclei, for example lithium-6 or -7, within the insertion electrode. As with XAS, NMR techniques are element specific (and nuclear specific) and do not require any long-range structural order in the host material for analysis. Solid-state NMR methods are now routinely employed to characterize the various chemical components of Li ion batteries: metal oxide cathodes, Li ion-conducting electrolytes, and carbonaceous anodes.^{248,249} Coupled to controlled electrochemical insertion/deinsertion of the NMR-active cations, the

chemical shifts of the ^6Li or ^7Li are used to distinguish between chemically distinct ion insertion sites within the host electrode structure, to differentiate electrochemically inactive Li ion sites, and to assess the mobilities of Li ions. Nuclear magnetic resonance studies of battery electrodes have recently been extended to in situ investigations of lithium insertion in carbon electrodes by Chevallier et al.²⁵⁰

6. Fabrication En Route to 3-D Integration of Architectural Components

6.1. Micromachining

The three-dimensional electrode arrays that are the basis for the interdigitated 3-D battery design (Figure 2a) have been fabricated successfully using different micromachining methods. Micromachining has emerged as an indispensable approach for fabricating materials into complex geometries.²⁵¹ These methods evolved from the realm of integrated circuits as researchers developed techniques for deposition, photolithographic patterning, and selective etching, among other processes. Distinctions can be drawn between bulk machining, where three-dimensional features are etched in bulk materials, and surface micromachining, where features are built up, layer-by-layer, on the surface of a substrate. Surface micromachining also involves the use of sacrificial films that are later dissolved to release the free-standing components. In both types of micromachining, photolithography serves as the basis for fabricating three-dimensional features.

Three-dimensional electrode arrays have been fabricated using two very different micromachining methods. One approach, named carbon MEMS or C-MEMS, is based on the pyrolysis of photoresists. The use of photoresist as the precursor material is a key consideration, since photolithography can be used to pattern these materials into appropriate structures. The second approach involves the micromachining of silicon molds that are then filled with electrode material. Construction of both anode and cathode electrode arrays has been demonstrated using these microfabrication methods.

6.1.1. Carbon MEMS (C-MEMS)

The synthesis and electrochemical properties of carbon films prepared from positive photoresist have been reported.^{252–254} The initial direction for this work was the fabrication of carbon interdigitated electrodes. In this work, positive photoresist was spin coated on a silicon substrate, patterned by photolithography, and pyrolyzed to form the carbon electrode. In more recent work, laser excitation has been used to both pyrolyze the film and to write the electrode pattern.²⁵⁵

The influence of pyrolysis conditions on the structure, morphology, electrical properties, and electrochemical behavior has been investigated. Raman spectroscopy shows that characteristic sp^2 carbon bands form from the pyrolysis treatments. The electrochemical properties for a few of the electrode systems have been reported and, for the most part,

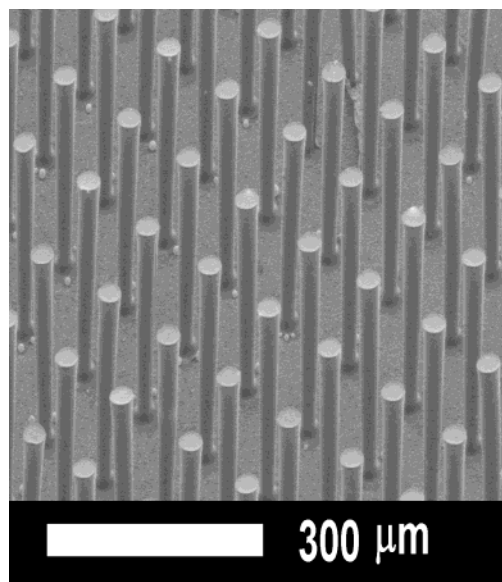


Figure 22. Array of carbon electrodes prepared by the C-MEMS process. The aspect ratio is approximately 20:1. (Courtesy of Prof. Marc Madou, University of California—Irvine.)

these pyrolyzed electrodes behave similarly to those of glassy carbon, a standard carbon electrode used in electrochemical studies. It is evident that good electrochemical responses are obtained for materials pyrolyzed at temperatures above 800 °C, although the best properties seem to occur at pyrolysis temperatures above 1000 °C. Voltammetric measurements show that the electron-transfer kinetics measured for $\text{Fe}(\text{CN})_6^{3-/4-}$ and $\text{Ru}(\text{NH}_3)_6^{3+/2+}$ are comparable to those determined for other carbon films and glassy carbon.²⁵⁴ One interesting difference with glassy carbon is that it is possible to prepare pyrolyzed carbon electrodes with lower oxygen content. The low oxygen content in the carbon film and its smooth surface are believed to be responsible for low capacitance ($8 \mu\text{F}/\text{cm}^2$), a feature that may be important for analytical applications.

Although these first studies were directed at 2-D interdigitated electrodes ($L/d \ll 1$) whose structures are not very useful for the proposed 3-D designs, it is apparent, nonetheless, that this microfabrication approach can be adapted for 3-D array electrodes. The recent work reported by Madou and colleagues demonstrated the types of electrode arrays that constitute the key design element for the interdigitated 3-D battery.¹⁷ By using a process similar to their initial work,²⁵⁴ but with a negative photoresist, carbon arrays with much higher L/d ratios were prepared, as shown in Figure 22.

The results by Madou et al. are especially significant, as they clearly demonstrate the ability to fabricate array electrodes with aspect ratios that are on the order of 20:1. At these aspect ratios, the analytical models indicate that the capacity of 3-D batteries exceeds that of 2-D geometries. Two key questions remain to be answered for C-MEMS: are these electrodes electrochemically reversible to lithium, and what is the resistance of rods with such high aspect ratios?

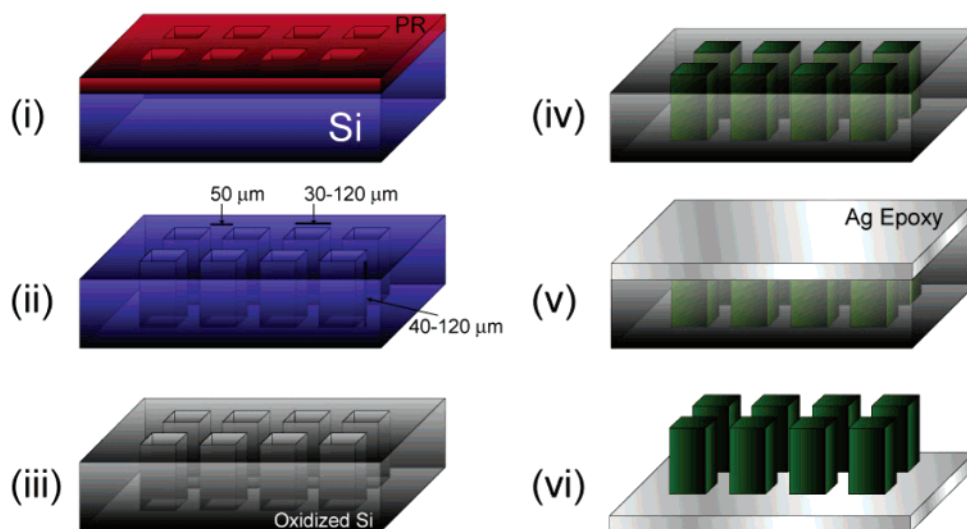


Figure 23. Processing flow for 3-D electrode array fabrication using silicon micromachining with colloidal filling of the electrode material. The six steps are identified as the following: (i) patterned photoresist (PR) on silicon substrate, (ii) PR removal after DRIE micromachining, (iii) insulate silicon mold by oxidation, (iv) colloidal electrode filling material centrifuged into the mold, (v) silver epoxy added to provide mechanical stability and electrical contact, (vi) the electrode flipped over and released from the mold by immersion in a TEOAH solution.

This first question concerning electrochemical properties has been answered in a series of half-cell experiments using the C-MEMS array as the working electrode and lithium as both the counter and reference electrode.²⁵⁶ In these experiments, reversible intercalation of lithium was demonstrated with C-MEMS array electrodes with an aspect ratio as high as 6:1. Voltammetric sweeps indicate that the electrochemical behavior is similar to that of coke electrodes as most of the lithium intercalation occurs below 0.5 V, with a broad deintercalation peak at 0.3 V. Galvanostatic measurements on the C-MEMS arrays show a large irreversible capacity loss on first discharge followed by good cycling properties, which is also consistent with the behavior of coke electrodes. The lithium capacity normalized to the footprint area of the electrode array is 0.125 mA h cm⁻². This value is nearly twice that of an unpatterned pyrolyzed film of SU-8 photoresist.²⁵⁶ The reason for the higher capacity is due to the greater active volume, contributed by the carbon posts, over the footprint area. Gravimetrically, these lithium capacities are within the range of values reported for coke electrodes. However, as discussed in the Introduction, the more relevant parameter to use in characterizing array electrodes is the lithium capacity per unit area of the array footprint.

The second key question—the resistance of carbon rods with high aspect ratios—is just beginning to be addressed. The first measurements made on individual pyrolyzed carbon rods with $L/d = 6$ and a diameter of $\sim 25 \mu\text{m}$ indicated resistance values on the order of 90–100 ohms. These measured values are reasonably consistent with calculated resistances based on the resistivity values reported for pyrolyzed photoresist. Future work that combines experiments with simulations will be able to establish how lithium capacity varies with aspect ratio.

6.1.2. Micromachining of Silicon Molds

A second approach for fabricating electrode arrays has involved micromachining of silicon molds,²⁵⁷ which are filled with electrode material by colloidal processing methods. In contrast to C-MEMS, this fabrication approach is suitable for both anodes and cathodes, as one merely alters the composition of the powders. The process flow for electrode array fabrication is depicted in Figure 23.

The silicon molds are prepared using photolithography and deep-reactive ion etching (DRIE). A 12- μm layer of photoresist is spin-coated onto a silicon wafer and patterned with an array of circles, ranging from 30–120 μm in diameter, 50 μm apart. The UV-exposed sections are dissolved away with developer and 40–120- μm -deep holes in the exposed areas of silicon are created by DRIE. From these dimensions, it was possible to explore the fabrication of electrode arrays of different L/d ratios. The mold is cleaned in a Piranha bath ($\text{H}_2\text{SO}_4/\text{H}_2\text{O}_2$ solution) and a 1 μm thick thermal oxide is grown on the silicon using wet oxidation at 1100 °C. The presence of the oxide layer helps in releasing the infiltrated electrode array.

The second step involves filling the silicon mold with the electrode powders. Several different active electrode powders were investigated including LiCoO_2 , carbon black, single-wall carbon nanotubes (SWNT), and vanadium oxide nanorolls (VONR). The active material is mixed with a binder (polyvinylidene fluoride, PVdF) in order to keep the array intact. The addition of binder is a standard procedure in the fabrication of battery electrodes, as is the addition of carbon black to improve the electronic conductivity of cathodes.¹ The silicon mold was placed in a vial containing a suspension of the electrode powders in ethylene glycol and then centrifuged, during which time the powders filled the silicon mold. The mold was removed from the vial and heated to 200 °C to evaporate the ethylene glycol and melt the PVdF,

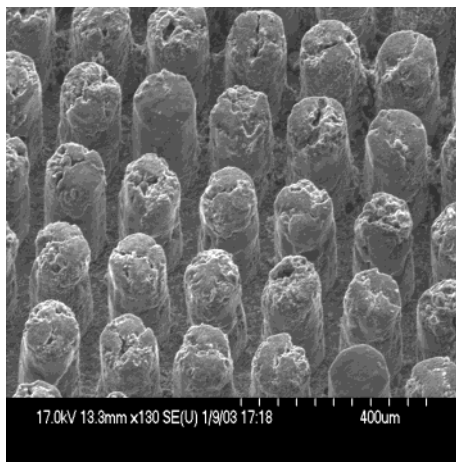


Figure 24. Electrode array prepared by the powder processing method shown in Figure 23. The electrode array structure is intact, although the individual rods contain defects.

thus binding the active electrode powders. Silver epoxy was spread over the back of the mold to maintain the mechanical integrity of the array as well as to provide electrical contact.

The final step in the process is to remove the electrode array from the silicon mold. This releasing function is accomplished by immersing the filled mold in an aqueous solution of tetraethylammonium hydroxide (TEAOH) heated to 80 °C. As the TEAOH begins to dissolve the silicon, the electrode array separates from the mold, usually as an intact piece. An SEM image of an array of vanadium oxide nanorolls is shown in Figure 24. It is evident from this photomicrograph that the fabrication process is far from perfect. The individual rods have defects including pores and cracks, and the arrays occasionally have missing rods.

The electrochemical properties of the micromachined electrode arrays have been determined for several of the electrode materials. In these half-cell experiments, the electrode array served as the working electrode and lithium as the counter and reference electrodes. The first experiments were carried out on carbon arrays composed of powders of Ketjen Black. Reversible intercalation and deintercalation of lithium were obtained, and reversible capacities in the range of 0.4–0.5 mA h cm⁻² were reported.²⁵⁷

Recent results with vanadium oxide nanorolls indicate that array electrodes prepared with these materials exhibit reversible intercalation of lithium and behave in much the same fashion as conventional VONR electrodes. Discharge curves for the first three cycles of a VONR array for $L/d = 3$ and a footprint area of 10 mm² are shown in Figure 25. The plateaus observed in these experiments are consistent with the results we obtained for well-ordered VONR powders.²⁵⁸ Figure 25 shows that the arrays exhibit good cycling properties and the lithium capacity normalized to the footprint area is ~ 1.5 mA h cm⁻². This electrode-area-normalized capacity is about 10 times higher than the value reported for thin-film cathodes.¹³ Once again the higher capacity for the footprint area is due to the greater volume contributed by the VONR posts.

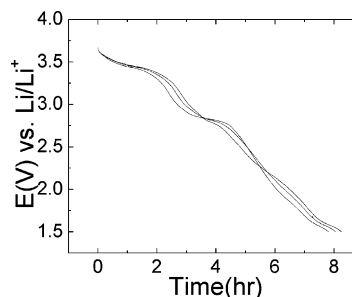


Figure 25. Discharge curves for the first three cycles for an electrode array composed of vanadium oxide nanorolls (see Figure 24). The current was 20 μ A and the footprint for the electrode array was 10 mm².

The micromachining of silicon molds is one key factor that determines the dimensions of the electrode array and, therefore, the energy of the 3-D battery. The use of electrochemical etching in HF to fabricate high-aspect-ratio trenches in silicon was introduced in 1990.²⁵⁹ Several groups have applied this technique in the fabrication of microstructures.²⁶⁰ Recently, Chamran et al. reported the use of this technique for 3-D microbattery fabrication.²⁶¹ The process flow is shown in Figure 26a. High intensity from the illumination source ensures that the electronic hole concentration is sufficiently high to sustain the etching process. The locations of the etched holes are determined by the initiation tips lithographically formed on top of the wafer before the photoelectrochemical etching starts. The narrow dimension concentrates the local electric field and ensures that etching occurs primarily at the tip. The resulting mold has etched holes with L/d ratios > 10 . The importance of high, localized fields for electrochemical micromachining has also been exploited to create precision features below 100 nm by using a sequence of 500-ps pulses.²⁶²

Calculations indicate that 3-D batteries constructed from electrode arrays with the dimensions shown in Figure 26b will be capable of providing over 2 mW h in a 5-mm³ package, an appropriate size and energy for powering MEMS devices. The holes are 5 μ m in diameter by 100- μ m-long and the center-to-center distance between holes is 10 μ m. For such dimensions, it is not known whether the colloidal processing approach described above will be effective, and it may be necessary to develop alternative powder-filling methods.

6.2. 3-D Fabrication Based on 2-D Structures: Origami

Another approach to forming 3-D electrode structures is based on various folding strategies. This "origami" approach was first reported for electronic and optoelectronic systems, as there is great interest in developing three-dimensional electronic networks and microelectronic devices. The folding of both planar²⁶³ and linear²⁶⁴ structures into 3-D configurations has been demonstrated; the adaptation of this work to electrochemical devices is just starting. Shao-Horn et al. reported on the assembly of 3-D electrochemical structures using patterned 2-D electrode sheets.¹⁸ The electrodes were designed to fold at

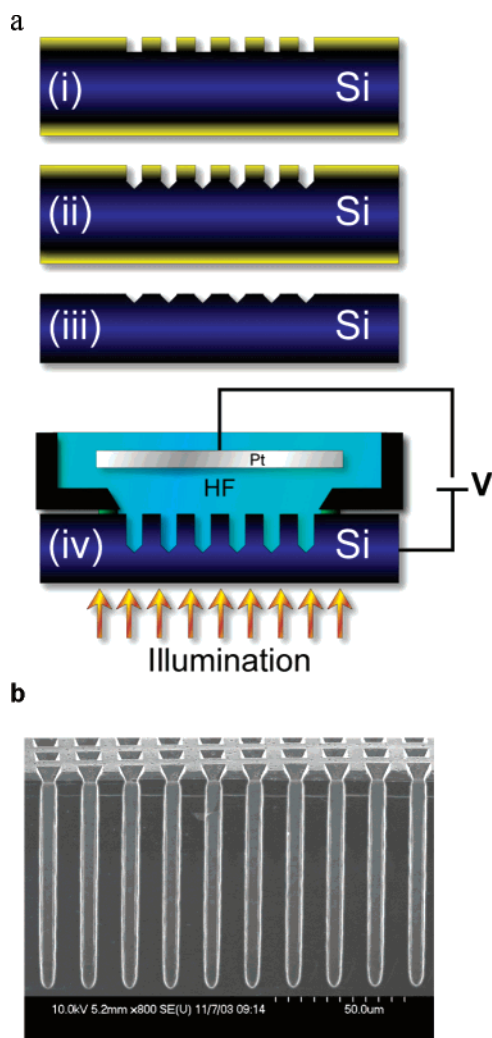


Figure 26. (a) Process flow for the fabrication of high-aspect-ratio holes in silicon as based on photoassisted etching: (i) thermal oxide is grown on n-Si and patterned; (ii) KOH etching through the holes; (iii) removal of oxide; and (iv) photoassisted anodic etching of silicon in HF. (b) Cross-section of silicon etched by the photoassisted process yielding an array of holes of 5- μm diameter by $\sim 100\text{-}\mu\text{m}$ -long; the center-to-center distance between holes is 10 μm .

specific creases based on the application of Lorentz forces. The 3-D structure is then assembled by the sequential folding of the 2-D electrode sheets. This work is clearly at its inception, as current efforts have only been able to achieve limited folding. Efforts are underway to demonstrate a 3-D capacitor structure.

The attractive feature of the origami approach is the prospect of using readily manufacturable 2-D patterning to form the electrochemical components. By proper folding, these 2-D components are then assembled into 3-D structures. The difficulty to date seems to be in the actual folding process. A significant difference between the 3-D electronic structures and the electrochemical structures is that the former rely on capillary forces from molten solder to achieve folding. As the liquid solder tries to minimize surface area, it self-assembles the 1-D or 2-D precursors into a 3-D structure. Upon cooling, the solder serves to provide both electrical connection and mechanical stability to the 3-D electronic network. The solder approach is not viable for electrochemical devices,

because the anode and cathode must be electrically isolated. Nonetheless, the use of capillary force to cause folding is attractive, and it would seem that there is an opportunity to use other materials with more compatible electrical properties. Much of the work done with conducting polymers that serve as actuators under various applied forces may also be adaptable to the origami effort.²⁶⁵

7. Advances toward Integration of Active Components into a 3-D Battery

7.1. Present Status

The construction of an operational, fully 3-D battery has yet to be achieved. However, as the previous sections have shown, on an individual basis, most of the active components for the 3-D designs presented in Figure 2 have been demonstrated successfully. Both anode and cathode array electrodes, the design elements that form the basis of the interdigitated battery (Figure 2a), have been fabricated and their electrochemical properties determined. The next key step is to carefully align these arrays so that interdigitation is achieved. The concentric tubule approach is also well along as carbon honeycomb electrode structures have recently been prepared.⁹⁷ These structures represent the continuous electrode phase (Figure 2c) and can serve as the porous membrane template, instead of alumina, for growing electrode materials.⁷⁴ One critical feature that needs to be resolved is the presence of an electrolyte that separates the two electrodes.

Of all the battery designs, it is the continuous sponge that is furthest along toward integrating components into a 3-D architecture (Figure 2d). This approach involves the design and fabrication of a three-dimensional network from the appropriate nanoscale building blocks, including the use of “nothing” (void space) and deliberate disorder as design components. A recent accomplishment in this area has been the electrodeposition of a conformal electrolyte layer on an aerogel substrate: complete integration of the electrode and electrolyte in a random 3-D network. The last step in the fabrication of this 3-D battery is to integrate an interpenetrating anode.

The importance of developing pinhole-free, electrolyte films of nanometer thickness is potentially useful for all 3-D battery designs. For this reason, most of this section reviews the synthesis and characterization of this ultrathin polymer electrolyte with an emphasis on topics such as leakage currents and dielectric strength, which become critically important at the nanoscale. A few comments concerning the packaging of 3-D batteries are made at the end.

7.2. Electrodeposition of Dielectrics—Separators and Cation-Conductive Electrolytes

One of the key steps en route to a 3-D nanoscopic battery requires fabricating an ultrathin film of a polymer separator/electrolyte over chemically stable, physically rugged, cation-insertion oxide scaffolds, such as supported films of MnOx ambipolymers.²⁰ In

keeping with our architectural metaphor, the fabrication protocol should be capable of painting the polymer as a conformal, ultrathin coating onto the walls of the battery building without protruding deeply into the rooms (and clogging the continuous porous network). The experiments underway create ultrathin, electronically insulating, cation-permeable films on charge-insertion oxide nanoarchitectures via electropolymerization of aryl monomers. The advantages of electropolymerizing aryl monomers include the ability to self-limit the growth of the electrogenerated polymer, usually by depositing from neutral or basic electrolytes, to yield thin (usually ~ 10 nm thick), poorly electron-conductive polymer layers that conformally coat all electrifiable surface area. Especially appealing in the design of interpenetrating 3-D batteries, electropolymerization provides a fabrication protocol that should be feasible within nanoarchitectures (unlike line-of-sight chemical vapor deposition approaches) and should ensure intimate contact at the electrode–polymer–electrolyte interface.

Such conformal, ultrathin polymer separators must satisfy a range of physical and chemical requirements in order to perform at the level necessary for charge insertion on the nanometer scale. These attributes include (i) highly electronically insulating, preferably $> 10^{-15}$ S cm $^{-1}$; (ii) pinhole-free to prevent electronic shorts between the charge-insertion cathode and the anode; (iii) ionically conducting to the charge-insertion ion (which in some designs may be a cation other than Li $^{+}$), preferably without the need for solvent or plasticizing molecules dissolved or partitioned into the polymer film; (iv) chemically nondegradable and electrochemically stable against Li metal, i.e., over a 3–4 V (vs Li) range; (v) forms a stable interface with metallic lithium, preferably without forming a highly resistive solid-electrolyte interphase layer; and (vi) exhibits a high dielectric strength, preferably $> 10^6$ V cm $^{-1}$.

The use of nanoscale (5–30-nm-thick) solid polymer electrolytes should significantly improve rate capabilities for batteries and other solid-state ionic devices and represents a considerable improvement over current micrometer-thick solid electrolytes used in thin-film batteries.^{13,266} The electro-oxidation of *o*-phenylenediamine in aqueous pH 9 electrolyte onto manganese oxide (MnO $_2$) ambigels produces a conformal polymer film that retains the mesoporosity of the original oxide and is so defect-free over the > 200 m 2 /g nanoscopic MnO $_2$ network that it prevents reductive dissolution of the MnO $_2$ nanoarchitecture upon immersion in aqueous acid.²⁰ Beyond serving as a protective coating, the poly(*o*-phenylenediamine) acts as a selective ion-transport membrane, where proton transport from the external electrolyte through the polymer coating is determined by the electrochemical state of the polymer, a phenomenon known as “electrochemical ion gating”.²⁶⁷

7.3. Hybrid Polymer–Aerogel Nanoarchitectures as Electrochemical Capacitors

The recognition that self-limited arylamine-based polymers could be electrochemically activated in aqueous acids has led to a new class of 3-D hybrid

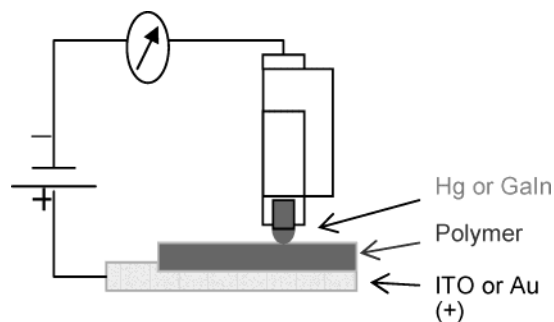


Figure 27. Schematic for solid-state electrical measurements with ultrathin polymer separators electrodeposited onto planar indium–tin oxide (ITO) or Au substrates. The top electrode makes a soft contact with the polymer by slow evaporation of Au or direct contact with a liquid metal (either Hg or GaIn eutectic) using a micrometer-controlled syringe to control the approach to contact. Measurements are made in an argon-filled glovebox to minimize effects of O $_2$ and H $_2$ O.

electrode structures. As mentioned previously, carbon aerogels are attractive electrode structures for electrochemical capacitors, because their open pore structures, high surface areas, and high electronic conductivities facilitate rapid charge–discharge reactions. However, carbon aerogels ultimately have very limited energy densities as electrochemical capacitors, since energy storage occurs primarily by the double-layer capacitance mechanism. This limitation has been addressed recently at the Naval Research Laboratory by the application of conformal, ultrathin poly(*o*-methoxyaniline) (POMA) coatings to conventional carbon aerogel electrodes. Preliminary experiments indicate that the addition of the pseudocapacitance of the POMA coatings increases the volumetric capacitance of the hybrid electrode structure by $\geq 200\%$, even at high rates of charge–discharge.²¹

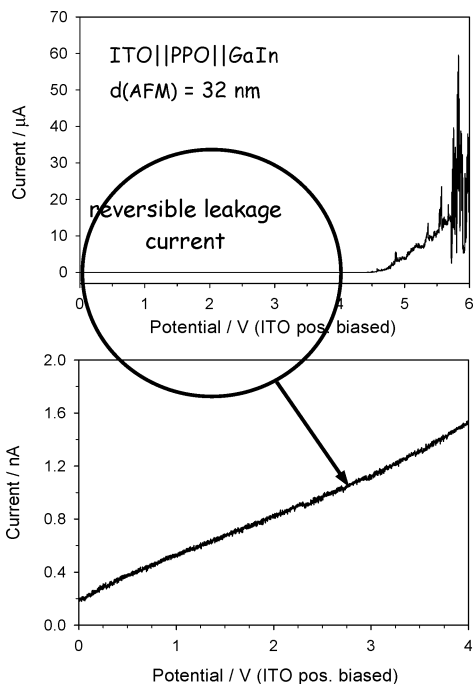
7.4. Solid-State Electrical Characterization of Conformal, Ultrathin Polymer Dielectrics

Although the literature on electrodeposited electroactive and passivating polymers is vast, surprisingly few studies exist on the solid-state electrical properties of such films, with a focus on systems derived from phenolic monomers,^{268,269} and apparently none exist on the use of such films as solid polymer electrolytes. To characterize the nature of ultrathin electrodeposited polymers as dielectrics and electrolytes, solid-state electrical measurements are made by electrodeposition of poly(phenylene oxide) and related polymers onto planar ITO or Au substrates and then using a two-electrode configuration with a soft ohmic contact as the top electrode (see Figure 27).²³ Both dc and ac measurements are taken to determine the electrical and ionic conductivities and the breakdown voltage of the film.

The electronic insulation of these electrodeposited polymer layers must hold to a two-terminal voltage of 4 V if lithium (or lithium ion) anodes are to be used in the 3-D nanobattery. Because the polymers must also be thin, high dielectric strengths are critical. As seen in Table 2, diminishing the thickness of the dielectric to the nanoscale exacts a higher standard in terms of the quality of the dielectric. For example,

Table 2. Required Dielectric Strengths for Nanometer-Thick Dielectrics

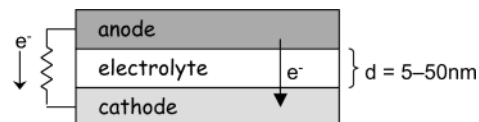
dielectric thickness/nm	field across dielectric at 3 V/(MV cm ⁻¹)
5	6
10	3
20	1.5
50	0.6

**Figure 28.** Solid-state dc electrical measurements of polyphenylene oxide in an ITO||PPO||GaIn sandwich. The thickness of the polymer was measured by tapping-mode atomic force microscopy. (Reprinted with permission from ref 23. Copyright 2004 American Chemical Society.)

placing 3 V across a 10 nm thick dielectric requires a material with a dielectric strength of 3×10^6 V cm⁻¹. Dielectrics do exist with that degree of field strength, e.g., quartz at 7×10^6 V cm⁻¹²⁷⁰ as well as polymers, e.g., poly(2,6-dimethylphenylene oxide) (PDPO) at 2.3×10^6 V cm⁻¹.²⁷¹

With an ITO||PPO||GaIn sandwich and the two-electrode configuration shown in Figure 27, a dielectric strength of $\geq 1.4 \times 10^6$ V cm⁻¹ is obtained for 32-nm-thick electrodeposited poly(phenylene oxide).²³ This value agrees with an estimated dielectric strength derived from previously reported current–voltage electrical data on 180-nm-thick poly(phenylene oxide).²⁶⁸ At voltages <4.5 V dc, the ohmic response in Figure 28 is stable; at applied voltages > 4.5 V dc, the current increases 4 orders of magnitude, from a few nanoamperes to tens of microamperes. Thus, 4.5 V dc is used to calculate an apparent dielectric strength.

The 10 000-fold increased currents at >4.5 V dc are not due to irreversible breakdown of the polymer dielectric, however, because an ohmic response is again obtained when $V_{\text{appl}} < 4.5$ V dc.²³ It appears that a reversible ion or atom migration, derived from the soft contact electrode, may be occurring. This possibility has recently been invoked to explain phenomena reported for certain molecular electronics

**Figure 29.** Schematic of the 1-D transport between an anode and cathode separated by an ultrathin, conformal polymer electrolyte.**Table 3. Self-Discharge Times for a 3-D Nanobattery as a Function of Electrolyte Thickness and Electrical Conductivity**

$\sigma_{\text{elec}}/\text{S cm}^{-1}$	thickness, d/nm	discharge time/h ^a
10^{-9}	5	10^{-5}
10^{-16}	5	10^2
10^{-16}	50	10^3

^a The calculation assumes a cathode structure with 50 μg of MnO_2 , 100 cm² of real electrode surface area, an electrode capacity of 120 mA h g⁻¹, and a 3 V operating voltage. Leakage current is calculated from the equation, $I_{\text{leak}} = V\sigma_{\text{elec}}A/d$, where V is the voltage and A is the electrode area. Discharge time is calculated by dividing capacity by the leakage current.

junctions formed at monomolecular layers between Au contacts.²⁷²

Ions can be introduced into these conformal, ultrathin polymers by exposure to nonaqueous electrolytes. Electrochemical cycling of the MnO_2 ||PPO hybrid in 1 M $\text{LiClO}_4/\text{CH}_3\text{CN}$ shows that Li ions are transported through the ~ 30 -nm-thick polymer film to the underlying metal oxide.²² Spectroelectrochemical measurements verify that the polymer-encapsulated mesoporous MnO_2 nanoarchitecture undergoes the normal cation-insertion reactions with Li ions from the external electrolyte; the charge under the voltammetric curves is comparable with and without the polymer.

7.5. Ultrathin Polymer Electrolyte—Leakage Currents

As discussed in section 2.5, one must be cognizant of the thickness of the dielectric/electrolyte that is sandwiched by the 3-D interpenetrating anode and cathode. Even with highly electronically insulating polymers, nanoscale distances that surpass those necessary to sustain quantum tunneling can lead to leakage currents, arising from small electrical conductivities at such short transport path lengths. For the 1-D transport characteristic of the aperiodic 3-D nanoarchitecture, as shown schematically in Figure 29, and with a dielectric thickness that falls below 0.1 μm , self-discharge can render 3-D nanobatteries useless, as shown in Table 3. The importance of negligible electronic conductivity for the dielectric cannot be overemphasized when the length scales are nanoscopic.

7.6. Last Step: Add an Interpenetrating Anode

Two-thirds of the assembly necessary to form the sponge architecture for a 3-D battery have now been demonstrated. By having a suitable pinhole-free, thin-to-ultrathin polymer barrier formed over the “walls” of the battery architecture, the remaining free volume can be filled with a counter electrode, as described above and depicted schematically in Figure

2d. The resulting architecture will be a solid-state, fully integrated 3-D battery. The use of mesoporous, high surface area aerogels and ambigels as substrates maximizes the interface between the cathode and anode, while the electrodeposited polymer minimizes the separation between the cathode and anode. In contrast to other 3-D designs, this nanostructure collapses to a uniform 2-D current density distribution and more effectively utilizes available volume.

7.7. Packaging of 3-D Batteries

A key issue that must be addressed in order for 3-D batteries to become viable for small power applications is packaging. The need to protect the battery in a volumetrically efficient package design without affecting battery materials or chemistry is a significant challenge. As discussed throughout this paper, MEMS devices represent an appropriate application where 3-D batteries could be well-utilized, and the prospect of developing a conveniently packaged power source, especially one attached to the backside of the device so that the real estate available for the micromachine is not reduced (see Figure 1), would be an attractive direction. It would seem, therefore, that packaging approaches for 3-D batteries should be those that lead to independently packaged components that can be readily integrated into portable power applications.

The packaging of 3-D batteries is likely to extend beyond those designs developed for lithium polymer and thin-film batteries. The packaging protocols developed for integrated circuit technologies appear to be extremely useful, since many of the objectives of IC packaging are identical to those of batteries.²⁵¹ Two approaches which are particularly attractive are the methods developed for single chip packages: chip carriers (ceramic or polymer) and TO (transistor outline) headers. Both approaches lead to hermetic sealing and conveniently interface the component to the "outside world". One advantage with batteries is that the wire bonding requirements for attaching leads is much less demanding than that of integrated circuits. The extensive experience with these approaches and the wide variety of packaging materials available ensure that the vital issue of process compatibility with battery chemistry and materials can be addressed successfully. The resulting packaged device, a "battery chip" designed to provide milliwatt-hour energies in cubic millimeter packages, could be readily integrated on microdevices for portable power.

8. Conclusions

One of the lessons learned in the 1990s was that the enormous need for high-performance portable power is not diminishing. Consumer electronics continues to be a vibrant, worldwide market force, leading to ever-increasing demands for portable power. The inability of lithium ion batteries to fully satisfy consumer electronics has been one of the principal motivations for the dramatic rise in fuel-cell research and development. As the dimensions of devices continue to shrink, the question arises as to

how power sources of comparable scale will be fabricated. The 2-D configurations of traditional batteries may not be effective here, despite their high energy density. Instead, energy conversion and harvesting approaches may be more suitable for powering microdevices, simply because of the ability to provide on-board power. These directions are being actively investigated.

Three-dimensional batteries offer a different approach to the portable power field. In this paper we have presented 3-D designs that emphasize power sources with small areal footprints but do not compromise power and energy density. While this approach may not help solve the power needs for cell phones and laptop computers, it will have a significant impact on current and future generations of microdevices. In particular, distributed sensor networks and wireless communication systems are representative areas where 3-D batteries would be welcomed enthusiastically because the power supplies currently in use are many times the size of the device.

This paper has established some of the design rules for 3-D batteries and the accompanying materials and fabrication strategies. The battery materials field is already beginning to explore 3-D concepts. Hierarchical designs based on nanostructured materials, including the deliberate management of void space, have been organized into larger macroscopic structures and the first results are impressive, with larger gravimetric capacities for lithium and higher discharge rates. It is because of this activity in materials that most of the necessary components for 3-D batteries are already in hand and the demonstration of the first operational 3-D batteries is imminent.

9. Acknowledgments

This work has been made possible by the support of the U. S. Office of Naval Research (ONR) and the Office of the Secretary of Defense through the Multidisciplinary University Research Initiative (MURI) on 3-D Microbatteries (under Grant N00014-01-1-0757). In particular, the authors would like to thank three visionary scientific officers at the ONR who during their various tenures advocated programs to explore electrochemical power from an integrated 3-D perspective: Robert Nowak, Richard Carlin, and Michele Anderson. We also wish to acknowledge the contributions of our insightful and productive colleagues: Christopher Rhodes [ONR-MURI postdoctoral associate (2002–2004)], Michael Doescher [NRC–NRL postdoctoral associate (2002–2005)], Rhonda Stroud (NRL), Christopher Smith, Ryan Hart, George Baure, Fardad Chamran, Jimmy Lim, Chai-Won Kwon, and Tim Yeh. We also appreciate the efforts of our colleagues who provided personal communications and allowed us to include some of their work: Prof. Marc Madou (University of California-Irvine), Prof. Kris Pister (University of California-Berkeley), Prof. C.-J. Kim (UCLA), and Prof. Sarah Tolbert (UCLA).

10. References

- (1) Wakihara, M. *Mater. Sci. Eng. R-Rep.* **2001**, *33*, 109.
- (2) Tarascon, J.-M.; Armand, M. *Nature* **2001**, *414*, 359.

- (3) Sadoway, D. R.; Mayes, A. M. *MRS Bull.* **2002**, *27*, 590.
- (4) Pescovitz, D. *Small Times* **2002**, *2*, 20.
- (5) Mullins, J. *IEEE Spectrum* **2001**, 23.
- (6) Lin, L. Y.; Wu, M. C.; Sawada, R.; Mohr, J. A. *J. Lightwave Technol.* **2003**, *21*, 582.
- (7) Niarchos, D. *Sensors Actuators A-Phys.* **2003**, *106*, 255.
- (8) Tilmans, H. A. C.; De Raedt, W.; Beyne, E. *J. Micromech. Microeng.* **2003**, *13*, S139.
- (9) Hartnagel, H. L.; Rodriguez-Girones, M. *IEICE Trans. Electron.* **2003**, *E86C*, 1911.
- (10) Mehregany, M.; Zorman, C. A. *MRS Bull.* **2001**, *26*, 289.
- (11) Koeneman, P. B.; Busch-Vishniac, I. J.; Wood, K. L. *J. Microelectromech. Sys.* **1997**, *6*, 355.
- (12) Kahn, J. M.; Katz, R. H.; Pister, K. S. J. *J. Commun. Networks* **2000**, *2*, 188.
- (13) Bates, J. B.; Dudney, N. J.; Neudecker, B.; Ueda, A.; Evans, C. D. *Solid State Ionics* **2000**, *135*, 33.
- (14) Note that $1 \text{ W h} = 3600 \text{ J}$, and a 2 J mm^{-3} energy density corresponds to $0.56 \text{ mW h mm}^{-3}$. The MEMS community reports energy units as J, whereas the battery community typically uses W h, and we will use the established conventions for energy units when discussing the work from these respective communities.
- (15) Souquet, J. L.; Duclot, M. *Solid State Ionics* **2002**, *148*, 375.
- (16) Warneke, B.; Last, M.; Liebowitz, B.; Pister, K. S. J. *IEEE Comput. Magazine* **2001**, *34*, 44.
- (17) Wang, C.; Taherabadi, L.; Randhawa, A.; Madou, M.; Kwon, C.-W.; Dunn, B. In *Abstracts of the 204th Meeting of the Electrochemical Society*; Electrochemical Society: Pennington, NJ, 2003; Abstr. #1276.
- (18) Shao-Horn, Y.; Hidrovo, C.; Jurga, S. M.; Smith, H. I.; Barbastathis, G. In *Abstracts of the 204th Meeting of the Electrochemical Society*; Electrochemical Society: Pennington, NJ, 2003; Abstr. #1279.
- (19) Hart, R. W.; White, H. S.; Dunn, B.; Rolison, D. R. *Electrochem. Commun.* **2003**, *5*, 120.
- (20) Long, J. W.; Rhodes, C. P.; Young, A. L.; Rolison, D. R. *Nano Lett.* **2003**, *3*, 1155.
- (21) Long, J. W.; Dening, B. M.; Rolison, D. R. *J. Non-Cryst. Solids* **2004**, in press.
- (22) Rhodes, C. P.; Long, J. W.; Doescher, M. S.; Dening, B. M.; Rolison, D. R. *J. Non-Cryst. Solids* **2004**, in press.
- (23) Rhodes, C. P.; Long, J. W.; Doescher, M. S.; Rolison, D. R. *J. Phys. Chem. B* **2004**, *108*, in press.
- (24) Smith, C. P.; White, H. S. Submitted for publication.
- (25) Boxley, C. J.; White, H. S.; Gardner, C. E.; Macpherson, J. V. *J. Phys. Chem. B* **2003**, *107*, 9677.
- (26) Bard, A. J.; Faulkner, L. R. *Electrochemical Methods*, 2nd ed.; John Wiley: New York, 2001.
- (27) Smith, C. P.; White, H. S. *Anal. Chem.* **1993**, *65*, 3343.
- (28) Levich, V. G. *Physicochemical Hydrodynamics*; Prentice Hall: New York, 1962.
- (29) Curtright, A. E.; Bouwman, P. J.; Wartena, R. C.; Swider-Lyons, K. E. *Int. J. Nanotechnol.* **2004**, *1*, 149.
- (30) *Approaches to Combat Terrorism (ACT): Opportunities for Basic Research, Joint Workshop by The Directorate of the Mathematical and Physical Sciences, NSF and the Intelligence Community*; National Science Foundation (http://www.mitre.org/public/act/10_22_final.pdf), 2003.
- (31) Priestnall, M. A.; Kotzeva, V. P.; Fish, D. J.; Nilsson, E. M. *J. Power Sources* **2002**, *106*, 21.
- (32) Dyer, C. K. *Nature* **1990**, *343*, 547.
- (33) Humble, P. H.; Harb, J. N.; LaFollette, R. *J. Electrochem. Soc.* **2001**, *148*, A1357.
- (34) Lee, S. J.; Chang-Chien, A.; Cha, S. W.; O'Hayre, R.; Park, Y. I.; Saito, Y.; Prinz, F. B. *J. Power Sources* **2002**, *112*, 410.
- (35) Kelley, S. C.; Deluga, G. A.; Smyrl, W. H. *AIChE J.* **2002**, *48*, 1071.
- (36) Kelley, S. C.; Deluga, G. A.; Smyrl, W. H. *Electrochem. Solid-State Lett.* **2000**, *3*, 407.
- (37) Yu, J.; Cheng, P.; Ma, Z.; Yi, B. *J. Power Sources* **2003**, *124*, 40.
- (38) Yu, J.; Cheng, P.; Ma, Z.; Yi, B. *Electrochim. Acta* **2003**, *48*, 1537.
- (39) Wainright, J. S.; Savinell, R. F.; Liu, C. C.; Litt, M. *Electrochim. Acta* **2003**, *48*, 2869.
- (40) Beebe, D. J.; Mensing, G. A.; Walker, G. M. *Annu. Rev. Biomed. Eng.* **2002**, *4*, 261.
- (41) Quake, S. R.; Scherer, A. *Science* **2000**, *290*, 1536.
- (42) Choban, E. R.; Markoski, L. J.; Stoltzfus, J.; Moore, J. S.; Kenis, P. A. *Power Sources Proc.* **2002**, *40*, 317.
- (43) Kummer, J. T.; Oei, D.-G. *J. Appl. Electrochem.* **1985**, *15*, 619.
- (44) Ferrigno, R.; Stroock, A. D.; Clark, T. D.; Mayer, M.; Whitesides, G. M. *J. Am. Chem. Soc.* **2002**, *124*, 12930.
- (45) Ferrigno, R.; Stroock, A. D.; Clark, T. D.; Mayer, M.; Whitesides, G. M. *J. Am. Chem. Soc.* **2003**, *125*, 2014.
- (46) Luo, T.-J. M.; Fei, J.; Lim, K. G.; Palmore, G. T. R. In *Nanotechnology and the Environment*; Karn, B., Masciangioli, T., Colvin, V. L., Alivisatos, A. P., Eds.; American Chemical Society: Washington, DC, 2004; in press.
- (47) Takeuchi, E. S.; Leising, R. A. *MRS Bull.* **2002**, *27*, 624.
- (48) Drews, J.; Wolf, R.; Fehrmann, G.; Staub, R. *J. Power Sources* **1999**, *80*, 107.
- (49) Chen, T.; Barton, S. C.; Binyamin, G.; Gao, Z. Q.; Zhang, Y. C.; Kim, H.-H.; Heller, A. *J. Am. Chem. Soc.* **2001**, *123*, 8630.
- (50) Mano, N.; Heller, A. *J. Electrochem. Soc.* **2003**, *150*, A1136.
- (51) Mano, N.; Mao, F.; Heller, A. *J. Am. Chem. Soc.* **2002**, *124*, 12962.
- (52) Mano, N.; Mao, F.; Heller, A. *J. Am. Chem. Soc.* **2003**, *125*, 6588.
- (53) Mano, N.; Mao, F.; Shin, W.; Chen, T.; Heller, A. *Chem. Commun.* **2003**, 518.
- (54) Kim, H.-H.; Mano, N.; Zhang, X. C.; Heller, A. *J. Electrochem. Soc.* **2003**, *150*, A209.
- (55) de la Garza, L.; Jeong, G.; Liddell, P. A.; Sotomura, T.; Moore, T. A.; Moore, A. L.; Gust, D. *J. Phys. Chem. B* **2003**, *107*, 10252.
- (56) Murata, K.; Izuchi, S.; Yoshihisa, Y. *Electrochim. Acta* **2000**, *45*, 1501.
- (57) Meyer, W. H. *Adv. Mater.* **1998**, *10*, 439.
- (58) Song, J. Y.; Wang, Y. Y.; Wan, C. C. *J. Power Sources* **1999**, *77*, 183.
- (59) Jones, S. D.; Akridge, J. R. *J. Power Sources* **1993**, *44*, 505.
- (60) Neudecker, B. J.; Zuhr, R. A.; Kwak, B. S.; Bates, J. B.; Robertson, J. D. *J. Electrochem. Soc.* **1998**, *145*, 4148.
- (61) Wang, B.; Bates, J. B.; Hart, F. X.; Sales, B. C.; Zuhr, R. A.; Robertson, J. D. *J. Electrochem. Soc.* **1996**, *143*, 3203.
- (62) Bates, J. B.; Dudney, N. J.; Lubben, D. C.; Gruzalski, G. R.; Kwak, B. S.; Yu, X.; Zuhr, R. A. *J. Power Sources* **1995**, *54*, 58.
- (63) Neudecker, B. J.; Dudney, N. J.; Bates, J. B. *J. Electrochem. Soc.* **2000**, *147*, 517.
- (64) Piqué, A.; Chrisey, D. B.; Auyeung, R. C. Y.; Fitz-Gerald, J.; Wu, H. D.; McGill, R. A.; Lakeou, S.; Wu, P. K.; Nguyen, V.; Duignan, M. *Appl. Phys. A* **1999**, *69*, S279.
- (65) Wartena, R.; Curtright, A. E.; Arnold, C. B.; Piqué, A.; Swider-Lyons, K. E. *J. Power Sources* **2004**, *126*, 193.
- (66) Kishida, K.; Kuriyama, K.; Nozaki, T. *Appl. Phys. Lett.* **2002**, *81*, 5066.
- (67) El-hami, M.; Glynne-Jones, P.; White, N. M.; Hill, M.; Beeby, S.; James, E.; Brown, A. D.; Ross, J. N. *Sensors Actuators A* **2001**, *92*, 335.
- (68) Ching, N. N. H.; Wong, H. Y.; Li, W. J.; Leong, P. H. W.; Wen, Z. *Sensors Actuators A* **2002**, *97-98*, 685.
- (69) Glynne-Jones, P.; Beeby, S. P.; White, N. M. *IEEE Proc.-Sci. Meas. Technol.* **2001**, *148*, 68.
- (70) Harb, J. N.; LaFollette, R. M.; Selfridge, R. H.; Howell, L. L. *J. Power Sources* **2002**, *104*, 46.
- (71) Abbott, E. A. *The Annotated Flatland—A Romance of Many Dimensions*; Perseus Publishing: Cambridge, MA, 2002.
- (72) Sing, K. S. W.; Everett, D. H.; Haul, R. A. W.; Moscou, L.; Pierotti, R. A.; Rouquerol, J.; Siemieniowska, T. *Pure Appl. Chem.* **1985**, *57*, 603.
- (73) Penner, R. M.; Martin, C. R. *J. Electrochem. Soc.* **1986**, *133*, 310.
- (74) Martin, C. R. *Chem. Mater.* **1996**, *8*, 1739.
- (75) Lakshmi, B. B.; Patrissi, C. J.; Martin, C. R. *Chem. Mater.* **1997**, *9*, 2544.
- (76) Sides, C. R.; Li, N. C.; Patrissi, C. J.; Scrosati, B.; Martin, C. R. *MRS Bull.* **2002**, *27*, 604.
- (77) Hulteen, J. C.; Martin, C. R. *J. Mater. Chem.* **1997**, *7*, 1075.
- (78) Martin, C. R.; Mitchell, D. T. In *Electroanalytical Chemistry*; Bard, A. J., Rubinstein, I., Eds.; Marcel Dekker: New York, 1999; Vol. 21.
- (79) Rouhi, A. M. *Chem. Eng. News* **2001**, *79*, 29.
- (80) Patrissi, C. J.; Martin, C. R. *J. Electrochem. Soc.* **1999**, *146*, 3176.
- (81) Patrissi, C. J.; Martin, C. R. *J. Electrochem. Soc.* **2001**, *148*, A1247.
- (82) Li, N. C.; Patrissi, C. J.; Che, G. L.; Martin, C. R. *J. Electrochem. Soc.* **2000**, *147*, 2044.
- (83) Nishizawa, M.; Mukai, K.; Kuwabata, S.; Martin, C. R.; Yoneyama, H. *J. Electrochem. Soc.* **1997**, *144*, 1923.
- (84) Li, N. C.; Martin, C. R. *J. Electrochem. Soc.* **2001**, *148*, A164.
- (85) Li, N. C.; Martin, C. R.; Scrosati, B. *Electrochem. Solid-State Lett.* **2000**, *3*, 316.
- (86) Li, N. C.; Martin, C. R.; Scrosati, B. *J. Power Sources* **2001**, *97-8*, 240.
- (87) Che, G.; Jirage, K. B.; Fisher, E. R.; Martin, C. R.; Yoneyama, H. *J. Electrochem. Soc.* **1997**, *144*, 4296.
- (88) Che, G.; Lakshmi, B. B.; Martin, C. R.; Fisher, E. R.; Ruoff, R. S. *Chem. Mater.* **1998**, *10*, 260.
- (89) Che, G. L.; Lakshmi, B. B.; Fisher, E. R.; Martin, C. R. *Nature* **1998**, *393*, 346.
- (90) Che, G. L.; Lakshmi, B. B.; Martin, C. R.; Fisher, E. R. *Langmuir* **1999**, *15*, 750.
- (91) Martin, C. R. *Acc. Chem. Res.* **1995**, *28*, 61.
- (92) Martin, B. R.; Dermody, D. J.; Reiss, B. D.; Fang, M. M.; Lyon, L. A.; Natan, M. J.; Mallouk, T. E. *Adv. Mater.* **1999**, *11*, 1021.
- (93) Nicewarner-Peña, S. R.; Freeman, R. G.; Reiss, B. D.; He, L.; Peña, D. J.; Walton, I. D.; Cromer, R.; Keating, C. D.; Natan, M. J. *Science* **2001**, *294*, 137.
- (94) Keating, C. D.; Natan, M. J. *Adv. Mater.* **2003**, *15*, 451.
- (95) Dewan, C.; Teeters, D. *J. Power Sources* **2003**, *119*, 310.

- (96) Masuda, H.; Watanabe, M.; Yasui, K.; Tryk, D.; Rao, T.; Fujishima, A. *Adv. Mater.* **2000**, *12*, 444.
- (97) Li, N. C.; Mitchell, D. T.; Lee, K. P.; Martin, C. R. *J. Electrochem. Soc.* **2003**, *150*, A979.
- (98) Stein, A.; Schroden, R. C. *Curr. Opin. Solid State Mater. Sci.* **2001**, *5*, 553.
- (99) John, S.; Busch, K. *J. Lightwave Technol.* **1999**, *17*, 1931.
- (100) Sakamoto, J. S.; Dunn, B. *J. Mater. Chem.* **2002**, *12*, 2859.
- (101) Stein, A. *Adv. Mater.* **2003**, *15*, 763.
- (102) Kang, S.; Yu, J. S.; Kruk, M.; Jaroniec, M. *Chem. Commun.* **2002**, 1670.
- (103) Gundiah, G.; Govindaraj, A.; Rao, C. N. R. *MRS Bull.* **2001**, *36*, 1751.
- (104) Yoon, S. B.; Kim, J. Y.; Yu, J.-S. *Chem. Commun.* **2001**, 559.
- (105) Zakhidov, A. A.; Baughman, R. H.; Iqbal, Z.; Cui, C. X.; Khayrullin, I.; Dantas, S. O.; Marti, I.; Ralchenko, V. G. *Science* **1998**, *282*, 897.
- (106) Zakhidov, A. A.; Khayrullin, I. I.; Baughman, R. H.; Iqbal, Z.; Yoshino, K.; Kawagishi, Y.; Tatsuhara, S. *Nanostructured Mater.* **1999**, *12*, 1089.
- (107) Lindén, M.; Schacht, S.; Schüth, F.; Steel, A.; Unger, K. K. *J. Porous Mater.* **1998**, *5*, 177.
- (108) Liu, T. B.; Burger, C.; Chu, B. *Prog. Polym. Sci.* **2003**, *28*, 5.
- (109) Soler-Illia, G. J. d. A. A.; Crepaldi, E. L.; Grosso, D.; Sanchez, C. *Curr. Opin. Coll. Interface Sci.* **2003**, *8*, 109.
- (110) Soler-Illia, G. J. d. A. A.; Sanchez, C.; Lebeau, B.; Patarin, J. *Chem. Rev.* **2002**, *102*, 4093.
- (111) Schüth, F. *Chem. Mater.* **2001**, *13*, 3184.
- (112) Yang, P. D.; Zhao, D. Y.; Margolese, D. I.; Chmelka, B. F.; Stucky, G. D. *Chem. Mater.* **1999**, *11*, 2813.
- (113) Mann, S.; Burkett, S. L.; Davis, S. A.; Fowler, C. E.; Mendelson, N. H.; Sims, S. D.; Walsh, D.; Whilton, N. T. *Chem. Mater.* **1997**, *9*, 2300.
- (114) Palmqvist, A. E. C. *Curr. Opin. Coll. Interface Sci.* **2003**, *8*, 145.
- (115) Gin, D. L.; Gu, W. Q.; Pindzola, B. A.; Zhou, W. J. *Acc. Chem. Res.* **2001**, *34*, 973.
- (116) Lin, H. P.; Mou, C. Y. *Acc. Chem. Res.* **2002**, *35*, 927.
- (117) Patarin, J.; Lebeau, B.; Zana, R. *Curr. Opin. Coll. Interface Sci.* **2002**, *7*, 107.
- (118) Forster, S. In *Colloid Chemistry I; Topics in Current Chemistry*; Antonietti, M., Ed.; Springer: Berlin, 2003; Vol. 226.
- (119) Schüth, F. *Angew. Chem., Int. Ed.* **2003**, *42*, 3604.
- (120) Ying, J. Y.; Mehnert, C. P.; Wong, M. S. *Angew. Chem., Int. Ed.* **1999**, *38*, 56.
- (121) Polarz, S.; Antonietti, M. *Chem. Commun.* **2002**, 2593.
- (122) Ryoo, R.; Joo, S. H.; Jun, S. *J. Phys. Chem. B* **1999**, *103*, 7743.
- (123) Yang, P. D.; Zhao, D. Y.; Margolese, D. I.; Chmelka, B. F.; Stucky, G. D. *Nature* **1998**, *396*, 152.
- (124) Grätzel, M. *J. Sol-Gel Sci. Technol.* **2001**, *22*, 7.
- (125) Wang, Y. D.; Ma, C. L.; Sun, X. D.; Li, H. D. *Appl. Catal. A-Gen.* **2003**, *246*, 161.
- (126) Wang, Y. D.; Ma, C. L.; Sun, X. D.; Li, H. D. *J. Non-Cryst. Solids* **2003**, *319*, 109.
- (127) Kavan, L.; Rathousky, J.; Grätzel, M.; Shklover, V.; Zukal, A. *Microporous Mesoporous Mater.* **2001**, *44*, 653.
- (128) Froba, M.; Muth, O.; Reller, A. *Solid State Ionics* **1997**, *101*, 249.
- (129) Kluson, P.; Kacer, P.; Cajthaml, T.; Kalaji, M. *J. Mater. Chem.* **2001**, *11*, 644.
- (130) Yun, H.-S.; Miyazawa, K.; Zhou, H. S.; Honma, I.; Kuwabara, M. *Adv. Mater.* **2001**, *13*, 1377.
- (131) Yoshitake, H.; Sugihara, T.; Tatsumi, T. *Chem. Mater.* **2002**, *14*, 1023.
- (132) Zheng, J.-Y.; Pang, J.-B.; Qiu, K.-Y.; Wei, Y. *J. Mater. Chem.* **2001**, *11*, 3367.
- (133) Nishimura, S.; Shishido, A.; Abrams, N.; Mallouk, T. E. *Appl. Phys. Lett.* **2002**, *81*, 4532.
- (134) Krtil, P.; Fattakhova, D.; Kavan, L.; Burnside, S.; Grätzel, M. *Solid State Ionics* **2000**, *135*, 101.
- (135) Kavan, L.; Attia, A.; Lenzmann, F.; Elder, S. H.; Grätzel, M. *J. Electrochem. Soc.* **2000**, *147*, 2897.
- (136) Ozkan, E.; Lee, S. H.; Liu, P.; Tracy, C. E.; Tepehan, F. Z.; Pitts, J. R.; Deb, S. K. *Solid State Ionics* **2002**, *149*, 139.
- (137) Cheng, W.; Baudrin, E.; Dunn, B.; Zink, J. I. *J. Mater. Chem.* **2001**, *11*, 92.
- (138) Attard, G. S.; Bartlett, P. N.; Coleman, N. R. B.; Elliott, J. M.; Owen, J. R.; Wang, J. H. *Science* **1997**, *278*, 838.
- (139) Nelson, P. A.; Owen, J. R. *J. Electrochem. Soc.* **2003**, *150*, A1313.
- (140) Nelson, P. A.; Elliott, J. M.; Attard, G. S.; Owen, J. R. *Chem. Mater.* **2002**, *14*, 524.
- (141) Liu, P.; Lee, S. H.; Tracy, C. E.; Yan, Y. F.; Turner, J. A. *Adv. Mater.* **2002**, *14*, 27.
- (142) Huang, L. M.; Wang, Z. B.; Wang, H. T.; Cheng, X. L.; Mitra, A.; Yan, Y. X. *J. Mater. Chem.* **2002**, *12*, 388.
- (143) Baeck, S. H.; Choi, K. S.; Jaramillo, T. F.; Stucky, G. D.; McFarland, E. W. *Adv. Mater.* **2003**, *15*, 1269.
- (144) Choi, K. S.; Lichtenecker, H. C.; Stucky, G. D.; McFarland, E. W. *J. Am. Chem. Soc.* **2002**, *124*, 12402.
- (145) Jun, S.; Joo, S. H.; Ryoo, R.; Kruk, M.; Jaroniec, M.; Liu, Z.; Ohsuna, T.; Terasaki, O. *J. Am. Chem. Soc.* **2000**, *122*, 10712.
- (146) Ryoo, R.; Joo, S. H.; Kruk, M.; Jaroniec, M. *Adv. Mater.* **2001**, *13*, 677.
- (147) Joo, S. H.; Jun, S.; Ryoo, R. *Microporous Mesoporous Mater.* **2001**, *44*, 153.
- (148) Kruk, M.; Jaroniec, M.; Kim, T. W.; Ryoo, R. *Chem. Mater.* **2003**, *15*, 2815.
- (149) Kim, T. W.; Park, I. S.; Ryoo, R. *Angew. Chem., Int. Ed.* **2003**, *42*, 4375.
- (150) Lee, J.; Yoon, S.; Oh, S. M.; Shin, C. H.; Hyeon, T. *Adv. Mater.* **2000**, *12*, 359.
- (151) Fuertes, A. B.; Nevskaja, D. M. *J. Mater. Chem.* **2003**, *13*, 1843.
- (152) Fuertes, A. B.; Nevskaja, D. M. *Microporous Mesoporous Mater.* **2003**, *62*, 177.
- (153) Yu, J. S.; Kang, S.; Yoon, S. B.; Chai, G. *J. Am. Chem. Soc.* **2002**, *124*, 9382.
- (154) Lu, A. H.; Schmidt, W.; Schüth, F. *New Carbon Mater.* **2003**, *18*, 181.
- (155) Lu, A. H.; Schmidt, W.; Spliethoff, B.; Schüth, F. *Adv. Mater.* **2003**, *15*, 1602.
- (156) Yoon, S. B.; Kim, J. Y.; Yu, J.-S. *Chem. Commun.* **2002**, 1536.
- (157) Yang, H. F.; Shi, Q. H.; Liu, X. Y.; Xie, S. H.; Jiang, D. C.; Zhang, F. Q.; Yu, C. Z.; Tu, B.; Zhao, D. Y. *Chem. Commun.* **2002**, 2842.
- (158) Kim, S. S.; Pinnavaia, T. J. *Chem. Commun.* **2001**, 2418.
- (159) Vix-Guterl, C.; Boulard, S.; Parmentier, J.; Werckmann, J.; Patarin, J. *Chem. Lett.* **2002**, 1062.
- (160) Han, B. H.; Zhou, W. Z.; Sayari, A. *J. Am. Chem. Soc.* **2003**, *125*, 3444.
- (161) Taguchi, A.; Smätt, J. H.; Lindén, M. *Adv. Mater.* **2003**, *15*, 1209.
- (162) Yoon, S.; Lee, J. W.; Hyeon, T.; Oh, S. M. *J. Electrochem. Soc.* **2000**, *147*, 2507.
- (163) Lee, J.; Yoon, S.; Hyeon, T.; Oh, S. M.; Kim, K. B. *Chem. Commun.* **1999**, 2177.
- (164) Zhou, H. S.; Zhu, S. M.; Hibino, M.; Honma, I. *J. Power Sources* **2003**, *122*, 219.
- (165) Soten, I.; Ozin, G. A. *Curr. Opin. Coll. Interface Sci.* **1999**, *4*, 325.
- (166) Yang, P. D.; Deng, T.; Zhao, D. Y.; Feng, P. Y.; Pine, D.; Chmelka, B. F.; Whitesides, G. M.; Stucky, G. D. *Science* **1998**, *282*, 2244.
- (167) Rolison, D. R.; Dunn, B. *J. Mater. Chem.* **2001**, *11*, 963.
- (168) Kistler, S. S. *Nature* **1931**, *127*, 741.
- (169) Hüsing, N.; Schubert, U. *Angew. Chem., Int. Ed. Engl.* **1998**, *37*, 23.
- (170) Pierre, A. C.; Pajonk, G. M. *Chem. Rev.* **2002**, *102*, 4243.
- (171) Harreld, J.; Wong, H. P.; Dave, B. C.; Dunn, B.; Nazar, L. F. *J. Non-Cryst. Solids* **1998**, *225*, 319.
- (172) Coustier, F.; Lee, J. M.; Passerini, S.; Smyrl, W. H. *Solid State Ionics* **1999**, *116*, 279.
- (173) Long, J. W.; Swider-Lyons, K. E.; Stroud, R. M.; Rolison, D. R. *Electrochem. Solid-State Lett.* **2000**, *3*, 453.
- (174) Long, J. W.; Stroud, R. M.; Rolison, D. R. *J. Non-Cryst. Solids* **2001**, *285*, 288.
- (175) Long, J. W.; Qadir, L. R.; Stroud, R. M.; Rolison, D. R. *J. Phys. Chem. B* **2001**, *105*, 8712.
- (176) Yamamoto, T.; Nishimura, T.; Suzuki, T.; Tamon, H. *Carbon* **2001**, *39*, 2374.
- (177) Xu, J. J.; Yang, J. S. *Electrochem. Commun.* **2003**, *5*, 230.
- (178) Yang, J. S.; Xu, J. J. *J. Power Sources* **2003**, *122*, 181.
- (179) Tamon, H.; Ishizaka, H.; Yamamoto, T.; Suzuki, T. *Drying Technol.* **2001**, *19*, 313.
- (180) Tamon, H.; Ishizaka, H.; Yamamoto, T.; Suzuki, T. *Carbon* **1999**, *37*, 2049.
- (181) Rolison, D. R. *Science* **2003**, *299*, 1698.
- (182) Passerini, S.; Ressler, J. J.; Le, D. B.; Owens, B. B.; Smyrl, W. H. *Electrochim. Acta* **1999**, *44*, 2209.
- (183) Salloux, K.; Chaput, F.; Wong, H. P.; Dunn, B.; Breiter, M. W. *J. Electrochem. Soc.* **1995**, *142*, L191.
- (184) Zhang, F.; Passerini, S.; Owens, B. B.; Smyrl, W. H. *Electrochem. Solid-State Lett.* **2001**, *4*, A221.
- (185) Chaput, F.; Dunn, B.; Fuqua, P.; Salloux, K. *J. Non-Cryst. Solids* **1995**, *188*, 11.
- (186) Coustier, F.; Passerini, S.; Smyrl, W. H. *J. Electrochem. Soc.* **1998**, *145*, L73.
- (187) Dong, W.; Rolison, D. R.; Dunn, B. *Electrochem. Solid-State Lett.* **2000**, *3*, 457.
- (188) Harreld, J. H.; Dong, W.; Dunn, B. *MRS Bull.* **1998**, *33*, 561.
- (189) Le, D. B.; Passerini, S.; Guo, J.; Ressler, J.; Owens, B. B.; Smyrl, W. H. *J. Electrochem. Soc.* **1996**, *143*, 2099.
- (190) Passerini, S.; Coustier, F.; Giorgetti, M.; Smyrl, W. H. *Electrochem. Solid-State Lett.* **1999**, *2*, 483.
- (191) Dong, W.; Dunn, B. *J. Non-Cryst. Solids* **1998**, *225*, 135.
- (192) Dong, W.; Dunn, B. *J. Mater. Chem.* **1998**, *8*, 665.
- (193) Dong, W.; Mansour, A. N.; Dunn, B. *Solid State Ionics* **2001**, *144*, 31.
- (194) Harreld, J. H.; Sakamoto, J.; Dunn, B. *J. Power Sources* **2003**, *115*, 19.
- (195) Owens, B. B.; Passerini, S.; Smyrl, W. H. *Electrochim. Acta* **1999**, *45*, 215.
- (196) Bock, V.; Emmerling, A.; Fricke, J. *J. Non-Cryst. Solids* **1998**, *225*, 69.

- (197) Schaefer, D. W.; Pekala, R.; Beaucage, G. *J. Non-Cryst. Solids* **1995**, *186*, 159.
- (198) Tamon, H.; Ishizaka, H.; Mikami, M.; Okazaki, M. *Carbon* **1997**, *35*, 791.
- (199) Frackowiak, E.; Beguin, F. *Carbon* **2001**, *39*, 937.
- (200) Li, W. C.; Reichenauer, G.; Fricke, J. *Carbon* **2002**, *40*, 2955.
- (201) Pekala, R. W.; Farmer, J. C.; Alviso, C. T.; Tran, T. D.; Mayer, S. T.; Miller, J. M.; Dunn, B. *J. Non-Cryst. Solids* **1998**, *225*, 74.
- (202) Koresh, J.; Soffer, A. *J. Electrochem. Soc.* **1977**, *124*, 1379.
- (203) Salitra, G.; Soffer, A.; Eliad, L.; Cohen, Y.; Aurbach, D. *J. Electrochem. Soc.* **2000**, *147*, 2486.
- (204) Kaneko, K. *J. Membr. Sci.* **1994**, *96*, 59.
- (205) Webb, P. A.; Orr, C. *Analytical Methods in Fine Particle Technology*; Micromeritics Instrument Corp.: Norcross, GA, 1997.
- (206) Fratzl, P. *J. Appl. Crystallogr.* **2003**, *36*, 397.
- (207) Göltner, C. G.; Smarsly, B.; Berton, B.; Antonietti, M. *Chem. Mater.* **2001**, *13*, 1617.
- (208) Smarsly, B.; Antonietti, M.; Wolff, T. *J. Chem. Phys.* **2002**, *116*, 2618.
- (209) Midgley, P. A.; Weyland, M. *Ultramicroscopy* **2003**, *96*, 413.
- (210) Terasaki, O.; Ohsuna, T.; Liu, Z.; Kaneda, M.; Kamiya, S.; Carlsson, A.; Tsubakiyama, T.; Sakamoto, Y.; Inagaki, S.; Che, S.; Tatsumi, T.; Cambor, M. A.; Ryoo, R.; Zhao, D.; Stucky, G.; Shindo, D.; Hiraga, K. In *Nanoporous Materials III, Studies in Surface Science and Catalysis*; Sayari, A., Jaroniec, M., Eds.; Elsevier: Amsterdam, 2002; Vol. 141.
- (211) de Jong, K. P.; Koster, A. J. *Chem. Phys. Chem.* **2002**, *3*, 776.
- (212) Thomas, J. M.; Terasaki, O.; Gai, P. L.; Zhou, W. Z.; Gonzalez-Cabret, J. *Acc. Chem. Res.* **2001**, *34*, 583.
- (213) Sakamoto, Y. H.; Kaneda, M.; Terasaki, O.; Zhao, D. Y.; Kim, J. M.; Stucky, G.; Shim, H. J.; Ryoo, R. *Nature* **2000**, *408*, 449.
- (214) Sakamoto, Y.; Diaz, I.; Terasaki, O.; Zhao, D. Y.; Pérez-Pariente, J.; Kim, J. M.; Stucky, G. D. *J. Phys. Chem. B* **2002**, *106*, 3118.
- (215) Kaneda, M.; Tsubakiyama, T.; Carlsson, A.; Sakamoto, Y.; Ohsuna, T.; Terasaki, O.; Joo, S. H.; Ryoo, R. *J. Phys. Chem. B* **2002**, *106*, 1256.
- (216) Carlsson, A.; Kaneda, M.; Sakamoto, Y.; Terasaki, O.; Ryoo, R.; Joo, S. H. *J. Electron Microsc.* **1999**, *48*, 795.
- (217) Fernandez, J. J.; Lawrence, A. F.; Roca, J.; Garcia, I.; Ellisman, M. H.; Carazo, J. M. *J. Struct. Biol.* **2002**, *138*, 6.
- (218) Engstrom, R. C. *Anal. Chem.* **1984**, *56*, 890.
- (219) Bard, A. J.; Fan, F.-R. F.; Mirkin, M. V. *Anal. Chem.* **1989**, *61*, 132.
- (220) Bard, A. J.; Fan, F.-R. F.; Mirkin, M. V. In *Electroanalytical Chemistry*; Bard, A. J., Ed.; Marcel Dekker: New York, 1994; Vol. 18.
- (221) Bath, B. D.; White, H. S.; Scott, E. R. *Imaging molecular transport across membranes*; John Wiley: New York, 2001.
- (222) *Scanning Electrochemical Microscopy*; Bard, A. J.; Mirkin, M. V., Eds.; John Wiley: New York, 2001.
- (223) Bath, B. D.; White, H. S.; Scott, E. R. *Anal. Chem.* **2000**, *72*, 433.
- (224) Fan, F.-R. F.; Bard, A. J. *Science* **1995**, *270*, 1849.
- (225) Miki, T.; Yanagi, H. *Langmuir* **1998**, *14*, 3405.
- (226) Macpherson, J. V.; Gueneau de Mussy, J.-P.; Delplancke, J.-L. *Electrochem. Solid-State Lett.* **2001**, *4*, E33.
- (227) Macpherson, J. V.; Jones, C. E.; Barker, A. L.; Unwin, P. R. *Anal. Chem.* **2002**, *74*, 1841.
- (228) Heineman, W. R. *J. Chem. Educ.* **1983**, *60*, 305.
- (229) Long, J. W.; Young, A. L.; Rolison, D. R. *J. Electrochem. Soc.* **2003**, *150*, A1161.
- (230) Talledo, A.; Granqvist, C. G. *J. Appl. Phys.* **1995**, *77*, 4655.
- (231) Rhodes, C. P.; Dong, W.; Long, J. W.; Rolison, D. R. In *Solid State Ionics IV*; Wachsman, E. D., Swider Lyons, K. E., Carolan, M. F., Garzon, F. H., Liu, M., Stetter, J. R., Eds.; Electrochemical Society: Pennington, NJ, 2003; Vol. PV2002-26.
- (232) Dong, W.; Long, J. W.; Rolison, D. R. Unpublished data, 2001, Naval Research Laboratory.
- (233) Parsons, J. G.; Aldrich, M. V.; Gardea-Torresdey, J. L. *Appl. Spec. Rev.* **2002**, *37*, 187.
- (234) de Groot, F. *Chem. Rev.* **2001**, *101*, 1779.
- (235) McBreen, J.; Balasubramanian, M. *JOM-J. Miner. Met. Mater. Soc.* **2002**, *54*, 25.
- (236) Balasubramanian, M.; Sun, X.; Yang, X. Q.; McBreen, J. *J. Power Sources* **2001**, *92*, 1.
- (237) Yoon, W. S.; Grey, C. P.; Balasubramanian, M.; Yang, X. Q.; McBreen, J. *Chem. Mater.* **2003**, *15*, 3161.
- (238) Yoon, W. S.; Kim, N.; Yang, X. Q.; McBreen, J.; Grey, C. P. *J. Power Sources* **2003**, *119*, 649.
- (239) Hwang, B. J.; Tsai, Y. W.; Santhanam, R.; Liu, D. G.; Lee, J. F. *J. Electrochem. Soc.* **2003**, *150*, A335.
- (240) Giorgetti, M.; Berrettoni, M.; Passerini, S.; Smyrl, W. H. *Electrochim. Acta* **2002**, *47*, 3163.
- (241) Giorgetti, M.; Passerini, S.; Smyrl, W. H.; Mukerjee, S.; Yang, X. Q.; McBreen, J. *J. Electrochem. Soc.* **1999**, *146*, 2387.
- (242) Giorgetti, M.; Mukerjee, S.; Passerini, S.; McBreen, J.; Smyrl, W. H. *J. Electrochem. Soc.* **2001**, *148*, A768.
- (243) Mansour, A. N.; Smith, P. H.; Baker, W. M.; Balasubramanian, M.; McBreen, J. *Electrochim. Acta* **2002**, *47*, 3151.
- (244) Mansour, A. N.; Smith, P. H.; Baker, W. M.; Balasubramanian, M.; McBreen, J. *J. Electrochem. Soc.* **2003**, *150*, A403.
- (245) Passerini, S.; Le, D. B.; Smyrl, W. H.; Berrettoni, M.; Tossici, R.; Marassi, R.; Giorgetti, M. *Solid State Ionics* **1997**, *104*, 195.
- (246) Livage, J. *Solid State Ionics* **1996**, *86-88*, 935.
- (247) Swider Lyons, K. E.; Love, C. T.; Rolison, D. R. *Solid State Ionics* **2002**, *152-153*, 99.
- (248) Grey, C. P.; Greenbaum, S. G. *MRS Bull.* **2002**, *27*, 613.
- (249) Grey, C. P.; Lee, Y. J. *Solid State Sci.* **2003**, *5*, 883.
- (250) Chevallier, F.; Letellier, M.; Morcrette, M.; Tarascon, J.-M.; Frackowiak, E.; Rouzaud, J. N.; Beguin, F. *Electrochem. Solid-State Lett.* **2003**, *6*, A225.
- (251) Madou, M. *Fundamentals of Microfabrication*; CRC Press: Baton Rouge, LA, 1997.
- (252) Kim, J.; Song, X.; Kinoshita, K.; Madou, M.; White, B. *J. Electrochem. Soc.* **1998**, *145*, 2314.
- (253) Kostecky, R.; Song, X. Y.; Kinoshita, K. *J. Electrochem. Soc.* **2000**, *147*, 1878.
- (254) Ranganathan, S.; McCreery, R.; Majji, S. M.; Madou, M. *J. Electrochem. Soc.* **2000**, *147*, 277.
- (255) Kostecky, R.; Song, X. Y.; Kinoshita, K. *Electrochem. Solid-State Lett.* **2002**, *5*, E29.
- (256) Wang, C.; Taherabadi, L.; Jia, G.; Madou, M.; Yeh, Y.; Dunn, B. *Electrochem. Solid-State Lett.* **2004**, in press.
- (257) Baure, G.; Kwon, C.-W.; Lee, G. G.; Chamran, F.; Kim, C.-J.; Dunn, B. In *Micropower and Microdevices*; Brandon, E. J., Ryan, A., Harb, J., Ulrich, R., Eds.; Electrochemical Society: Pennington, NJ, 2002; Vol. PV2002-25.
- (258) Sun, D.; Kwon, C.-W.; Baure, G.; Richman, E.; MacLean, J.; Dunn, B.; Tolbert, S. H. Submitted for publication.
- (259) Lehmann, V.; Foll, H. *J. Electrochem. Soc.* **1990**, *137*, 653.
- (260) Foll, H.; Christophersen, M.; Carstensen, J.; Hasse, G. *Mater. Sci. Eng. R-Rep.* **2002**, *39*, 93.
- (261) Chamran, F.; Christophersen, M.; Kim, C.-J. In *Abstracts of the 204th Meeting of the Electrochemical Society*; Electrochemical Society: Pennington, NJ, 2003; Abstr. #1292.
- (262) Kock, M.; Kirchner, V.; Schuster, R. *Electrochim. Acta* **2003**, *48*, 3213.
- (263) Gracias, D. H.; Kavthekar, V.; Love, J. C.; Paul, K. E.; Whitesides, G. M. *Adv. Mater.* **2002**, *14*, 235.
- (264) Whitesides, G. M.; Boncheva, M. *Proc. Natl. Acad. Sci. U.S.A.* **2002**, *99*, 4769.
- (265) Smela, E. *Adv. Mater.* **2003**, *15*, 481.
- (266) Jang, Y. I.; Dudney, N. J.; Blom, D. A.; Allard, L. F. *J. Electrochem. Soc.* **2002**, *149*, A1442.
- (267) Burgmayer, P.; Murray, R. W. *J. Am. Chem. Soc.* **1982**, *104*, 6139.
- (268) Dubois, J.-E.; Tourillon, G.; Pham, M.-C.; Lacase, P.-C. *Thin Solid Films* **1980**, *69*, 141.
- (269) McCarty, R. L.; Thomas, R. E.; Irene, E. A.; Murray, R. W. *J. Electroanal. Chem.* **1990**, *290*, 79.
- (270) Whitehead, S. *Dielectric Breakdown of Solids*; Oxford University Press: Oxford, UK, 1953.
- (271) Adohi, B.; Gosse, J. P.; Gosse, B. *J. Phys. III* **1991**, *1*, 1623.
- (272) Service, R. F. *Science* **2003**, *302*, 556.

CR020740L